Simulation of the Part-Load Behavior of a 30 MWe SEGS Plant

Frank Lippke
Solar Thermal Technology Department

SAND95-1293

Printed June 1995

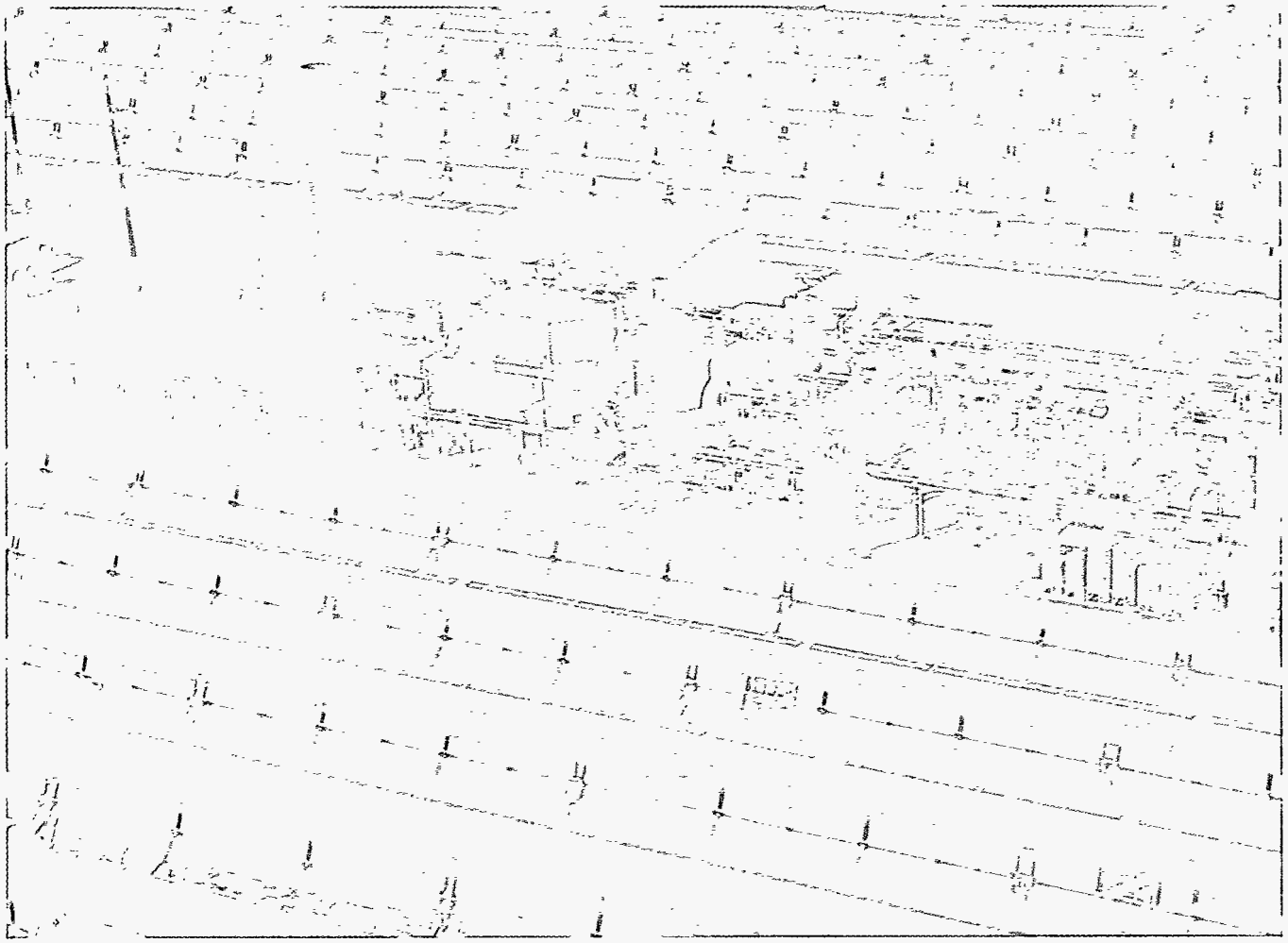

Department of Energy

Sandia National Laboratories

Issued by Sandia National Laboratories, operated for the United States Department of Energy by Sandia Corporation.

Available to DOE and DOE contractors from
Office of Scientific and Technical Information
PO Box 62
Oak Ridge, TN 37831

Prices available from (615) 576-8401, FTS 626-8401

Available to the public from
National Technical Information Service
US Department of Commerce
5285 Port Royal Rd
Springfield, VA 22161

NTIS price codes
Printed copy: A05
Microfiche copy: A01

SAND95-1293
Unlimited Release
Printed June 1995

Distribution Category
UC-1302
UC-1303

Simulation of the Part-Load Behavior of a 30 MWe SEGS Plant

Frank Lippke
Solar Thermal Technology Department
Sandia National Laboratories
Albuquerque, New Mexico 87185

Abstract

The part-load behavior of a typical 30-MWe SEGS plant was studied using a detailed thermodynamic model. As part of this analysis, a new solar field model was derived, based on measurement results of an LS-2 Collector and accounting for various conditions of receiver tubes, lost mirrors and measured reflectivity.

A comparison was made of the model results to real plant conditions for a winter and summer day in order to test the accuracy of the model. The effects of bare tubes, different wind speeds, mirror reflectivity and other factors were studied showing, e.g., that heat losses due to wind are predicted to be very low. The comparison also shows that the model still lacks the capability to fully account for actual solar field conditions. The model was also compared to the SOLERGY model, showing differences between the assumptions used in both models.

Finally different operating conditions of the plant were studied for a summer, fall, and winter day to provide a better understanding of how changing solar field outlet temperatures affect gross and net output of the plant. This clearly indicates that the lowest possible superheating temperature maximizes the gross electric output. On a net basis this conclusion is modified due to the high parasitics of the HTF pumps. It was found that the optimum operating strategy depends on the insolation conditions, e.g., different superheating temperatures should be chosen in summer, fall and winter. If the pressure drop in the solar field is reduced due to replacement of flex hoses with ball joints, increasing the HTF flow is more reasonable, so that at low insolation conditions the lowest possible superheating temperature also leads to the maximum net output.

Acknowledgment

I would like to thank

Greg J. Kolb, for always taking his time to discus assumptions and results,

KJC OC for providing the data needed for comparison of the results,

Robert Cable, Gilbert Cohen and Dave Kearney for their support and discussion of the results, and

Rainer Ratzesberger for implementing the solar field model into the EASY code.

I also would like to thank Anne Van Arsdall for providing helpful suggestions to the report, and thank Tech Reps for formatting the manuscript.

Contents

List of Figures

List of Tables

Nomenclature

A = coefficient
A_{SF} = solar field aperture area
B = coefficient
C = coefficient
D = coefficient
e_{mo} = pump curve parameter
f = focal length
I = direct insolation
Ia = incident angle
K = incident modifier
k = heat transfer coefficient
k_m = dependency coefficient
k_o = heat transfer coefficient at design conditions
k_p = friction factor
l_{SCA} = length of an Solar Collector Assembly
M = end loss factor
m = mass flow rate
m_o = design mass flow rate
p = pressure
Δp = pressure drop
Q_{abs} = absorbed power
$Q_{\text{Expansion Vessel}}$ = expansion vessel heat losses
$Q_{\text{Heat Losses}}$ = heat losses
Q_{Piping} = piping heat losses
ΔT = temperature difference between ambient and bulk temperature
v_{wind} = wind speed
z = length

η_{bare} = thermal efficiency of bare HCE tubes
η_s = turbine stage efficiency
η_{so} = turbine stage efficiency at design conditions
η_{th} = thermal efficiency
Φ_A = degradation factor
Φ_E = cleanliness factor for glass envelope
Φ_M = cleanliness factor
ψ_i = weighting factor
$\varphi_{\text{lost Mirrors}}$ = percentage of broken mirrors throughout the solar field
$\Delta\vartheta_{SF}$ = solar field outlet temperature

1. Introduction

In order to project the annual performance of solar electric plants, simulation programs using simplified energy transfer models such as SOLERGY (Stoddard et al., 1987) or the FLAGSOL model (Flachglas Solartechnik, 1994) have been developed. These programs account for the most important variables that influence the electricity generated, such as the solar field performance and turbine start-up times, so that is possible to predict the electricity production of different systems at different locations. The programs therefore provide important information for future erection of plants.

To increase the output of existing plants, more detailed models are necessary, since the results now depend not only on the actual plant conditions but also on the operating strategy of the plant. For this, thermodynamic models for heat exchangers, turbine stages, condenser, and other power cycle components have to be included in the calculations. One example of a simulation program that can be used for detailed calculations of flow cycles is the EASY code (Wahl, 1992). This program provides the possibility of calculating any user-defined flow cycle and examining different operating conditions.

In this study EASY is used to simulate the plant performance of a SEGS plant operating in the pure solar mode. A model for the solar field used in the calculations is derived from measurements for a LS-2 Collector. The results are compared to measured plant data so that both the accuracy of the model for the Rankine cycle as well as the applicability of the solar field model to represent the plant conditions will be shown. The model is also compared to the SOLERGY model, which gives important hints for future improvements of this simplified model.

Different operation strategies are compared in order to know how the output of the plant can be maximized. Such different operation modes can be the highest possible solar field outlet temperature, a constant mass flow rate through the solar field, or in general different main steam superheating temperatures. It is also possible to change the Rankine cycle by taking out feedwater heaters. As the operating conditions depend on the radiation, the comparison is made for three characteristic days in summer, spring/fall and winter.

2. EASY Model for the 30 MWe SEGS Plant

The 30 MWe solar electric generating systems (SEGS) located at Kramer Junction and operated by KJC Operating Company consist of two separate major subsystems: the solar field and the turbine-generator (Fig. 1). In the first subsystem thermal oil as the heat transfer fluid (HTF) is circulated through the solar field and used in heat exchangers to produce steam for a conventional Rankine cycle. In the second system - the Rankine cycle

- an additional gas-fired boiler is also used to run the plant when no or insufficient solar energy is available.

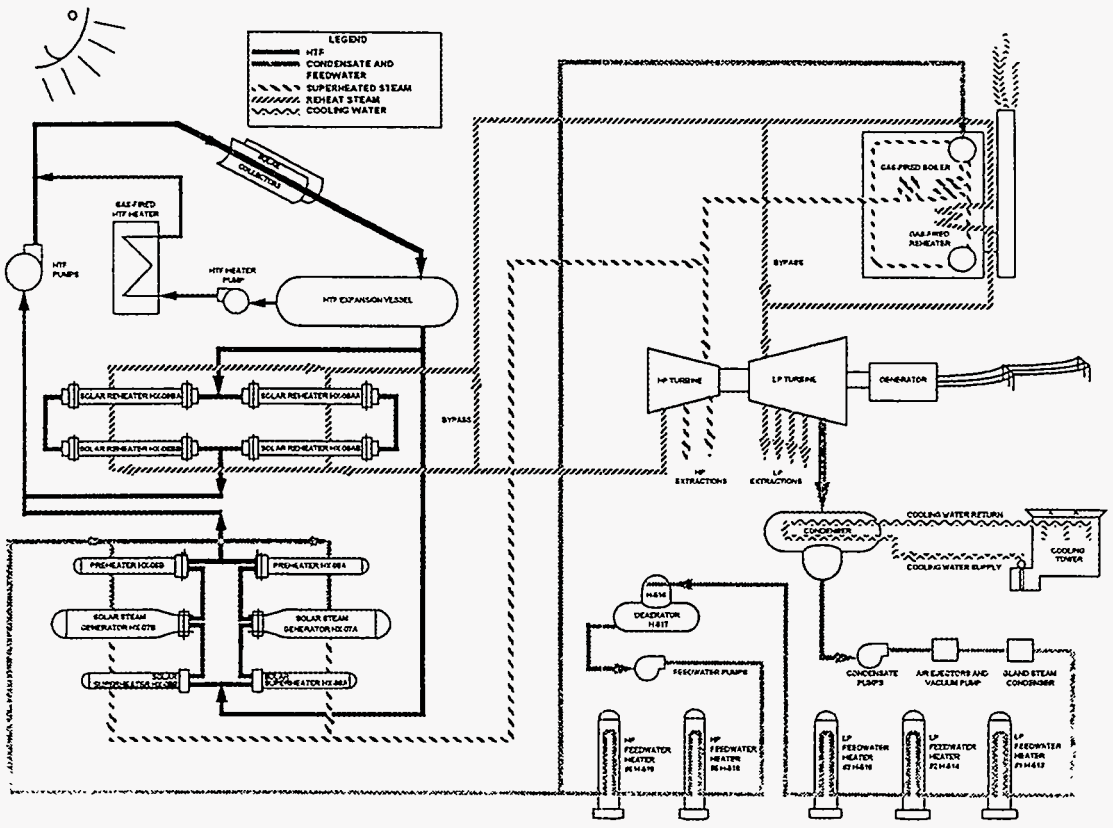

Fig. 1: Flow Diagram of a typical 30 MWe SEGS Plant (Miller, 1992)

Figure 2 shows how this flow cycle can be divided into components and streams in the EASY model if pure solar operation is considered. In the model, the two parallel solar heat exchanger trains shown in Fig. 1 are treated together and, for reasons of simplicity and because the results aren't affected much by this change, only the main three low pressure (LP) preheaters are considered in the Rankine cycle. Heat losses in all the piping in the solar field and in those of the huge expansion vessel are accounted for by an additional heat exchanger (named pipeLosses) at the outlet of the solar field.

As can be seen in Fig. 2 the model includes two leakage streams, one before the high pressure (HP) turbine, the other before the inlet of the LP turbine. One intent was to study the influence of increasing leakages, which was not done in this study but can be done later if necessary. Since the condensate and the feed water pump are operated at constant speed, the plant control valves are needed to reduce the pressure at the outlet of these pumps. In addition to these two valves, another is installed at the inlet of the HP turbine to control the main steam pressure if desired. Note that leakage and constant main steam pressure are only included in the calculations to compare the results with design calculations.

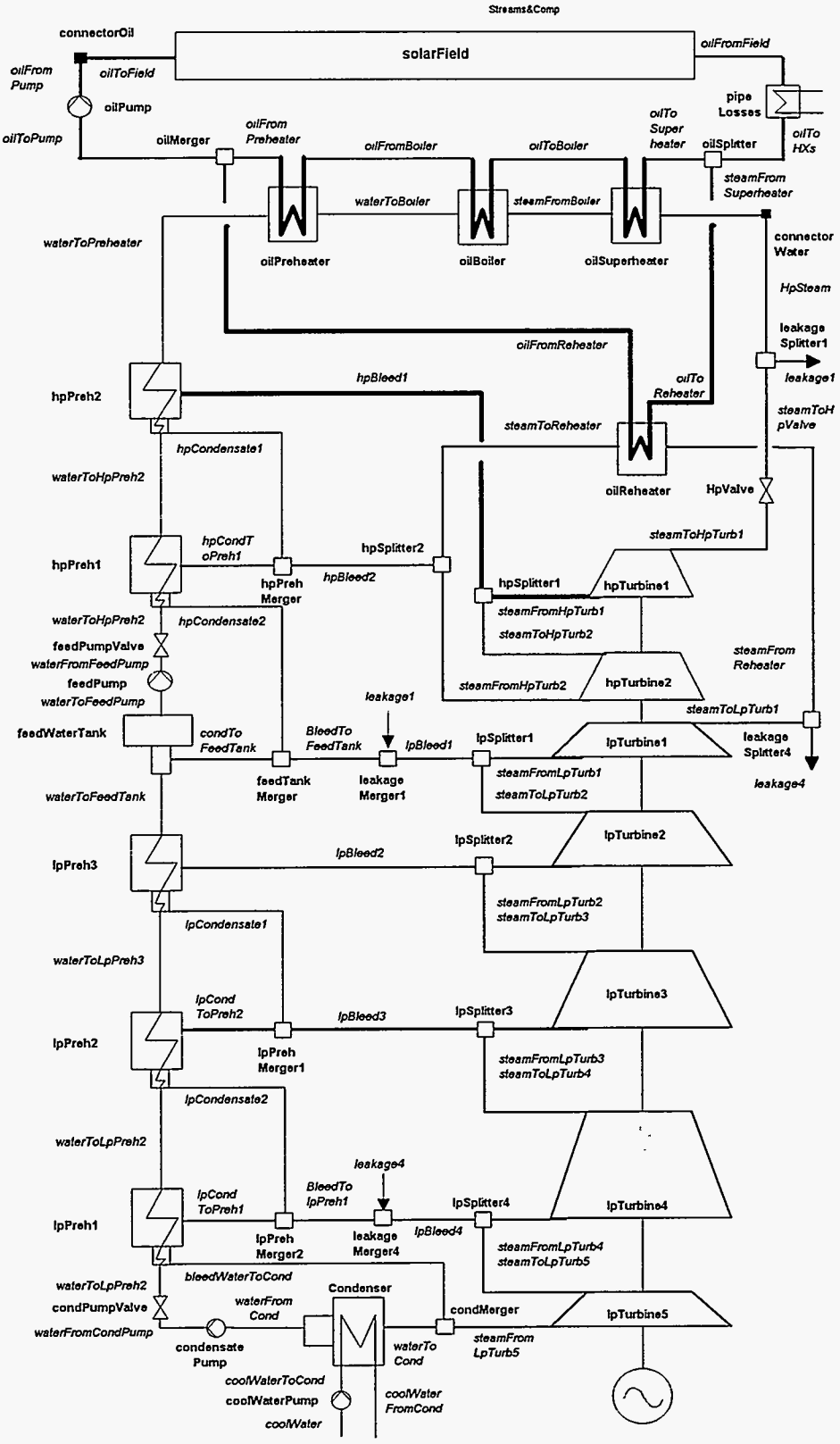

Fig. 2: EASY Model for the SEGS Plant (Components--bold, Streams--italic)

3. Model Parameters for Design Conditions

3.1. Parameters for the Components

Prior to a detailed analysis of a plant performance, the input parameters needed in the model, such as heat exchange areas, heat transfer coefficients, pressure drop dependencies, turbine stage efficiencies, etc. have to be defined. In EASY these input parameters are divided into design values and part load dependencies. The design values are therefore needed first. Since in EASY all parameters can be treated as variables, it is possible to calculate these out of flow conditions known or by defining a reasonable and sufficient set of water-steam properties along the Rankine cycle. Such water-steam properties, for example,. are the temperatures and pressures along the main water-steam path, the pressures and enthalpies of the extraction streams and the pressures and the qualities (saturated water) of the extraction streams having passed the preheaters. EASY then calculates all necessary internal design parameters such as the turbine stage design efficiencies or the overall heat transfer coefficients of the heat exchangers.

For this study, the necessary properties can be taken out of the technical description (Kearney et al., 1988) where water-steam conditions throughout the Rankine cycle are given for different operating conditions, e.g., different solar loads or with additional gas-firing. From the cases presented there, the VP4 mode with 100% pure-solar load (gross output = 35 MWe) is considered to be the design case. Figure 3 shows the heat balance for this case (see Appendix A for all diagrams in English units).

The HTF temperatures and the pressures throughout the solar cycle are taken either from the Operations Manual (LUZ Engineering Corporation, 1989) or the technical description. In order to describe the pressure loss of the solar field accurately (this is done in EASY using the Moody equations) the measured pressure drop of about 300 PSI (KJC Operating Company, 1994) at maximum flow is used and the roughness of the solar field piping is adjusted to match this.

In analyzing the available data, it appeared that the information provided was not always consistent. One example is the last LP-extraction stream for which a specific enthalpy lower than the LP outlet enthalpy is given. Because of this, the efficiency of the fourth LP turbine stage cannot be calculated (considering the enthalpy at the last extraction), but the enthalpy must be determined assuming a reasonable turbine stage efficiency for the fourth stage. In this study, 88% is used for this stage efficiency. This causes the overall efficiency to be slightly higher than mentioned in the technical description of the plant.

In analyzing the pure solar heat rates of the feasibility study, it can also be found that a generator efficiency of 97% is included in the data. This must also be accounted for in the EASY calculations.

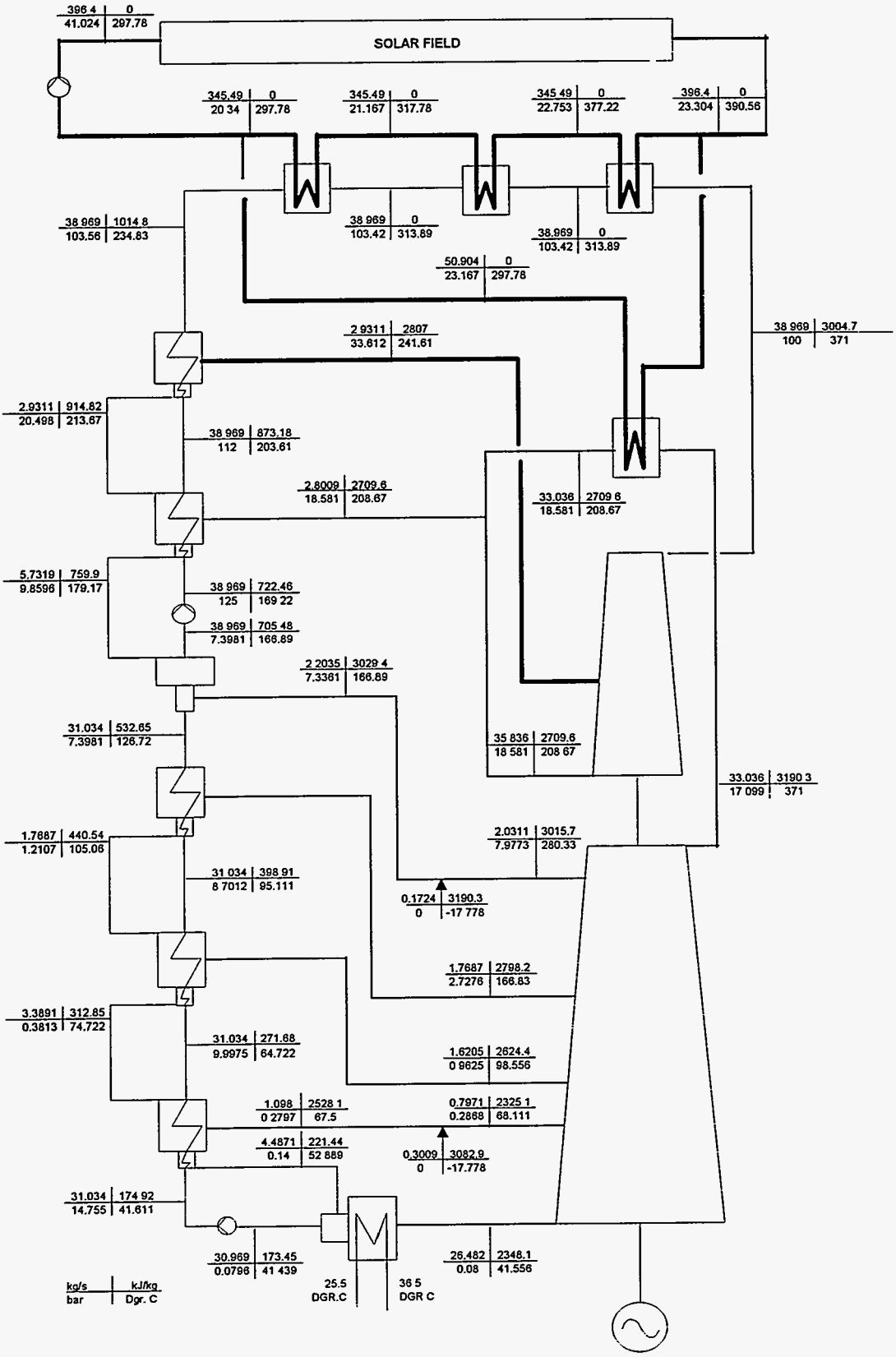

Fig. 3: Design Heat Balance at 100% Solar Load (Kearney et al., 1988)

3.2. Plant Parasitics and Pump Efficiencies

In characterizing the plant's performance, the plant parasitics play an important role. In the thermodynamic cycle, these are mainly those of the pumps and the cooling tower fans, and only these are included in the calculation. All other parasitics have to be accounted for "outside" the results; this study ignores them.

For the description of the part-load behavior of the pumps, it is assumed, that they reach their optimum efficiency at the design flow rate - this is also assumed for all other components of the plant such as turbine stages, heat exchangers, etc. This is not necessarily true, but no better information was available for this study. No design information was available on pump efficiencies, so reasonable values had to be used. The efficiencies used in this analysis, which are adopted to the design data, are summarized in Table 1.

Table 1: Pump Efficiencies

	Description	pump efficiency	motor efficiency	variable speed drive efficiency
condensatePump	Condensate Pump	0.75	0.95	
feedPump	Feedwater Pump	0.75	0.95	
oilPump	HTF Pump	0.75	0.95	0.95
coolWaterPump	Cooling Water Pump	0.75	0.95	

As there is no model for the cooling tower available in EASY yet, the power consumption of the fans must be treated in the calculations by adding their parasitics to the parasitics of the cooling water pump. This can be done by increasing the pressure drop of the cooling water cycle so that the parasitics in design load are equal to the sum of the parasitics of the cooling water pumps and the fans.

3.3. Simulation Results

Figure 4 shows the EASY result for the heat balance at 100% pure solar (VP4) operation. Comparing the results with the design conditions (Fig. 3), it can be seen that most of the water-steam conditions in the Rankine cycle match the design heat balance quite well. This is, of course, not possible for those locations where inconsistent data (as mentioned in Chapter 3.1) were found.

Considerably different from the design conditions and also from real plant operation is the HTF flow rate predicted by the EASY model. The reason for this is that the specific heat capacity of the HTF included in EASY[1] is slightly higher than actual, resulting in a lower mass flow rate through the solar field. However the part load predictions shouldn't be affected by this if the lower mass flow rate is considered as a "numerical design value". Then temperature and pressure drop dependencies are again treated accurately.

[1] The functions included in EASY to describe the properties weren't changed during this study since only an executable was provided by ZSW.

The predicted parasitics of the pumps are given in Table 2. The values are close to the design parasitics of the HTF pump and a little too low for the balance-of-plant equipment.

Table 2: Calculated Pump Parasitics

	Calculated Parasitics MWe	Design Values, MWe (Kearney et al., 1989)
condensatePump + feedPump	0.19 + 0.88 = 1.07	1.50
oilPump (HTF Pump)	1.56	1.60
coolWaterPump	0.99	0.91

Due to the necessary adaptation of the LP turbine stage efficiency, the gross electric efficiency of the predicted Rankine cycle is 38.2%; this is a little higher than the 37.5% presented in the technical description. The net energy output at 100% solar operation becomes 31.4 MWe.

In Table 3 all the component design parameters are summarized. It shows that the roughness of the solar field piping, including the effect of flex hoses, is calculated to be 1.9mm and that the efficiencies of the turbine stages are within a reasonable range.

Table 3: Design Parameters adopted by EASY (see Section 4)

```
solarField.l             = 753.6000[m] ; solarField.di        =    0.0650[m];
solarField.da            =   0.0700[m] ; solarField.roughness =    0.0019[m];
solarField.numberOfPipes =  50.0000[-] ; solarField.tAmb      =   30.0000[°C];

feedWaterTank.kpCold     =  20.6848[-] ; feedWaterTank.kpHot  = 1127.5664[-];

             (    kpCold,      kpHot,       A*k0,     mHot0, mCold0);
             (       [-],        [-],     [kW/K],      [kg], [kg/s]);
oilPreheater   :132.5543,     0.8956,    48.8084,  316.9956, 38.8435;
oilSuperheater :132.5543,     0.5971,   282.2158,  316.9956, 38.8435;
oilReheater    :135.0186,     8.7249,   478.9268,   47.8779, 33.1081;
hpPreheater1   :860.8224,      28479,   839.8529,    5.5334, 38.8435;
hpPreheater2   :397.6629,     154930,   663.1151,    2.9089, 38.8435;
lpPreheater1   :491.0749,  720.4526,   456.7598,    4.4831, 31.0949;
lpPreheater2   :134.4515, 5094.1179,   642.3171,    3.3778, 31.0949;
lpPreheater3   :124.1091,      48907,   191.7188,    1.7612, 31.0949;
Condenser      :  0.4824,     0.5171,  7418.6914,   31.0949, 1133.6929;

oilBoiler.kpCold =     132.5543[-];                    (  etas0,  mFeed0);
oilBoiler.kpHot  =       1.4927[-];                    (    [-],  [kg/s]);
oilBoiler.A      =  2699.1843[m^2];      condensatePump : 0.7125,   31.09;
oilBoiler.k0     = 1.000[kW/m^2/K];      feedPump       : 0.7125,   38.84;
oilBoiler.mHot0  =    316.9956[kg];      oilPump        : 0.6769,  364.87;
oilBoiler.mCold0 =     38.8435[kg];      coolWaterPump  : 0.7125,  113369;

          ( mFeed0,   pFeed0, pDrain0,  etas0,genPower);
          ( [kg/s],    [bar],   [bar],    [-],   [kW]);
hpTurbine1:38.6415, 100.0000, 33.6100, 0.8376, 7643.538;
hpTurbine2:35.7326,  33.6100, 18.5800, 0.8463, 3480.355;
lpTurbine1:32.8068,  17.1000,  7.9770, 0.8623, 5730.183;
lpTurbine2:30.7936,   7.9770,  2.7280, 0.9170, 6697.607;
lpTurbine3:29.0324,   2.7280,  0.9625, 0.9352, 5045.830;
lpTurbine4:27.4158,   0.9625,  0.2868, 0.8800, 4505.279;
lpTurbine5:26.6117,   0.2868,  0.0800, 0.6445, 2979.683;
```

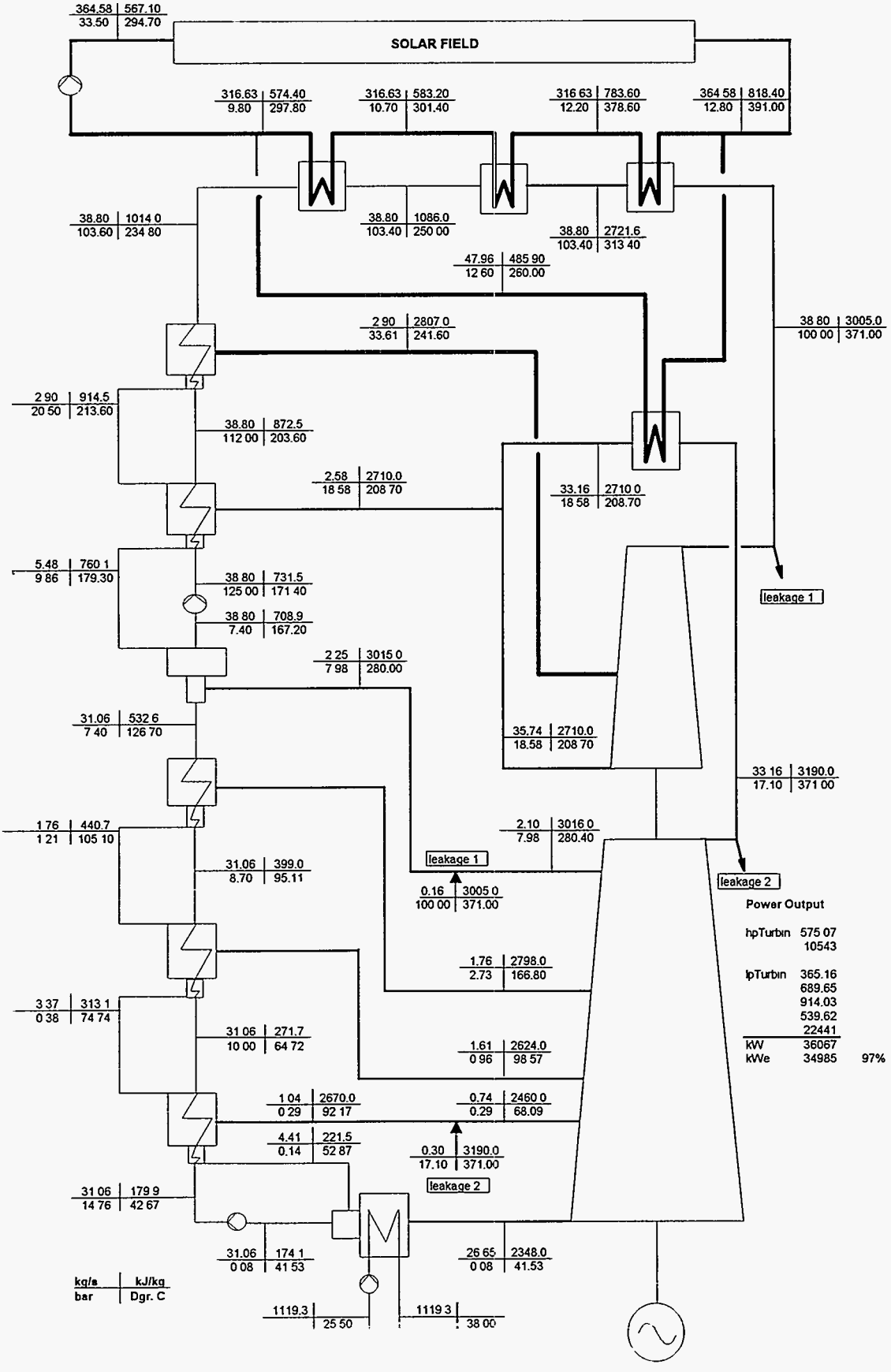

Fig. 4: EASY Results for the Heat Balance at 100% Solar Load.

4. Modeling Part Load Characteristics of Components

The second step in modeling the plant is to define the parameters that describe the part load characteristics of the components. Here it is necessary to know about the models included in the calculations. These are described briefly in the following section starting with the solar field, the most important one.

4.1. Solar Field Thermal Performance

4.1.1. LS-2 Performance Equation

The solar field thermal performance model is based on tests conducted by Sandia National Laboratories for an LS-2 Collector on the rotating platform (Dudley et al., 1994). From the results of these tests, efficiency equations were derived for HCEs with vacuum, air in the annulus, or for bare tubes as a function of fluid temperature, incident angle, insolation and, for bare tubes, of wind speed.

In defining the thermal efficiency, η_{th}, of the collector as the ratio of absorbed power (in %), Q_{abs}, to the direct normal insolation, I (in W/m^2), the general equation

$$\eta_{\text{th}} = \frac{Q_{abs}}{I} = K\left[A + B(\Delta T)\right] + C\frac{\Delta T}{I} + \text{D}\frac{\Delta T^2}{I} \qquad (1)$$

was found to be adequate for the description of all HCE conditions except for bare tubes. In this equation, A accounts for the optical efficiency of the trough and the absorbtivity of the selective coating without considering the losses at the end of a collector row (see Chapter 4.2). B, C and D describe the heat losses of the HCE dependent on its conditions with ΔT as the temperature difference between the HTF and the ambient in degrees Kelvin. The incident modifier, K, is a function of the incident angle Ia:

$$K = \cos(Ia) - 0.0003512(Ia) - 0.00003137(Ia)^2 \quad . \qquad (2)$$

For bare tubes, no dependency on insolation was found but there was a strong influence by the wind. The following equation is given for Cermet as the selective coating:

$$\eta_{bare} = 74.7 - 0.042(\Delta T) - 0.000731(\Delta T)^2 - 0.00927(\Delta T)v_{wind} \qquad (3)$$

which can be transformed to a form similar to Eq. (1)

$$\eta_{bare} = K\left[\underbrace{74.7}_{A_{bare}} \underbrace{-\left(0.042 + 0.00927\frac{v_{wind}}{K}\right)}_{B_{bare}}(\Delta T)\right] \underbrace{+0}_{C_{bare}}(\Delta T) \underbrace{-0.000731}_{D_{bare}}(\Delta T)^2 \quad . \qquad (4)$$

Table 4 summarizes the parameters as they were found in the test results.

Table 4: LS-2 Thermal Performance Coefficients

	A	B	C	D
Cermet, vacuum	73.3	-0.007276	-0.496	-0.0691
Cermet, air	73.4	-0.004683	-14.40	-0.0637
Cermet, bare	74.7	-0.042-0.00927*v_{Wind}/K	0.00	-0.000731*I
Black Chrome, Vacuum	73.6	-0.004206	7.44	-0.0958
Black Chrome, air	73.8	-0.006460	-12.16	-0.0641

4.1.2. Solar Collector Assembly End Losses

The efficiency equations derived by Dudley et al. (1994) do not include the end losses of a parabolic trough row. These are simply a function of the focal length, f, of the collector and the incident angle, Ia, as shown in Fig. 5.

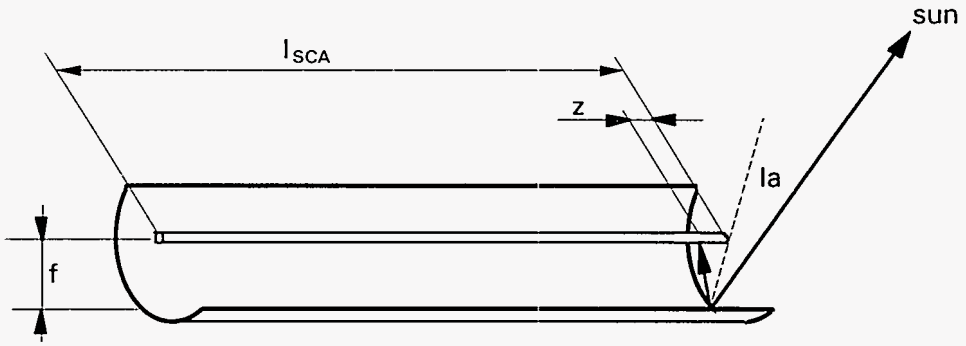

Fig. 5: End Losses of a Collector Row

The receiver length, z, which is not illuminated by the sun, then is

$$z = f\tan(Ia) \quad . \qquad (5)$$

Relative to the total length, l_{SCA}, of the solar collector assembly (SCA), the amount of heat concentrated on the whole receiver tube therefore has to be reduced by the factor M

$$M = \frac{l_{SCA} - z}{l_{SCA}} = 1 - \frac{f\tan(Ia)}{l_{SCA}} \quad . \qquad (6)$$

M has to be included in Eq. (1) so that this becomes[2]

$$\eta_{th} = KM\left[A + B(\Delta T)\right] + C\frac{\Delta T}{I} + \mathrm{D}\frac{\Delta T^2}{I} \qquad (7)$$

4.1.3. Performance Equation Considering Different HCE Conditions

In the calculations carried out in this study, not every HCE in the solar field is treated separately. Only a single element with a performance equation like Eq. (1) is used. The parameters for this equation therefore have to account for the different HCE types found in the field as well as for broken mirrors and, what has not been mentioned yet, "fluorescing" tubes. For the latter HCE type, the coating is defective and partially coats the inner wall of the glass envelope which then reflects the concentrated light so that no or only a little sunlight reaches the absorber tube. This means that such HCEs, which still cause heat losses, can be approximated by using zero for factor A in Eq. (1). The same is true for HCEs whose mirrors are broken.

Another important factor to be included in the calculations is the cleanliness of the mirrors, ϕ_M. Measurements show that the reflectivity of the mirrors drops considerably between two washing cycles without rain. The measured data can be used to get ϕ_M by comparing it to the maximum reflectivity achieved right after a wash - which is about 90.5% for the LS-2 Collector (Kolb[#], 1994):

$$\Phi_M = \frac{actual\ reflectivity}{maximum\ reflectivity} \quad . \qquad (8)$$

Dirt also reduces the transmittance of the glass envelope, but no information is available on that. A reasonable assumption, however, is that the cleanliness or the reduction in transmissivity of the mirrors and the glass envelopes is about the same. Since light has to pass two times through dirt on the mirrors (reflective side at the back of the glass) and one time through the glass envelope, the cleanliness factor for the glass envelope, ϕ_E, can be calculated by

$$\Phi_E = \frac{1 + \Phi_M}{2} \quad . \qquad (9)$$

Finally, when setting up the parameters for the performance equation, the influence of each HCE type must be weighted. Considering the percentage ψ_i of HCEs of a particular

---

[2] As an example for an LS-2 Collector (f = 1.49m, l_{SCA} = 47.1m), the factor M becomes 94.9% at noon on January 1 (Ia = 58°).

[#] see footnote 5, page 20

state and the assumption that all types of HCEs are distributed homogeneously over the solar field this can be done by[3] :

$$A_{Field} = \left(A_{Bare}\psi_{Bare} + \Phi_E \sum_{i,j \neq Bare} A_i \psi_i \right) \left(1 - \varphi_{Lost\ Mirrors}\right) \Phi_M \Phi_A \tag{10}$$

$$B_{Field} = \sum_i B_i \psi_i \tag{11}$$

$$C_{Field} = \sum_i C_i \psi_i \tag{12}$$

$$D_{Field} = \sum_i D_i \psi_i \tag{13}$$

with ϕ_A as an additional factor that can be used to vary the overall optical efficiency or modify the overall absorptivity and $\varphi_{Lost\ Mirrors}$ as the percentage of broken mirrors throughout the solar field. Note, that

$$\sum_i \psi_i = \quad \psi_{C,Vac} + \psi_{BC,Vac} + \psi_{C,air} + \psi_{BC,air} + \psi_{bare} + \psi_{fluor} = \tag{14}$$

applies (with C=Cermet, BC=Black Chrome).

4.2. Piping and Expansion Vessel Heat Losses

In the operation of a distributed solar power plant, the heat losses in all the piping are important and have to be included in the model. Additionally, the heat losses in the expansion vessel, which has a large surface area, should be included in the calculations. Both heat losses are treated in the EASY model through the heat exchanger named "pipeLosses" at the outlet of the solar field, as shown in Fig. 2.

Both heat losses are considered to be temperature dependent, which is different from the SOLERGY model, where a constant solar field outlet temperature is assumed. The following dependency was implemented in the model

$$\begin{aligned} \dot{Q}_{Heat\,Losses} &= \dot{Q}_{Piping} + \dot{Q}_{ExpansionVessel} \\ &= 20\frac{W}{m^2} A_{SF} \frac{\overline{\Delta\vartheta}_{SF}}{343^o C} + 2.57 MW_{th} \frac{\overline{\Delta\vartheta}_{SF}}{275^o C} \end{aligned} \tag{15}$$

[3] Example: If 88% of the HCEs are intact, 3.0% contain air, 7.4% are bare tubes, 1.6% have defective coatings and 0.18% of mirrors are broken the performance parameters for HCEs with Cermet become: A=72.1, B =-0.00977 - 0.000686 v_{Wind} / K, C =-0.8786, D =-0.0638 - 5.4094e-6 * I

Here, heat losses of all the piping of 20W per square meter aperture area, A_{SF}, are assumed at full solar power at a mean solar field temperature above ambient of about $\overline{\Delta\vartheta_{SF}} = 343°C$ (649°F) (Kolb, 1994). The radiation and mixed convection heat losses of the expansion vessel were estimated to be 2.57MW_{th} at 300°C (572°F) field outlet temperature (275°C mean field temperature) assuming poor insulation conditions experienced in the plant under consideration in 1994.

4.3. Turbine Stages

EASY accounts for changes in the efficiencies of turbine stages during part load by modifying the design efficiency η_{so} dependent on the pressures p_1 and p_2 at the inlet and outlet of the stage:

$$\frac{\eta_s}{\eta_{so}} = 1 + \alpha\left(\frac{p_1 / p_{10}}{p_2 / p_{20}} - 1\right)^2 \tag{16}$$

with p_{10} and p_{20} as the design values. In the calculations only a slight dependency for all stages, $\alpha = 0.1$, is assumed. The pressure difference over a turbine stage is calculated by

$$\frac{\dot{m}^2}{\dot{m}_0{}^2} = \frac{p_1^2 - p_2^2}{p_{10}^2 - p_{20}^2} \quad . \tag{17}$$

4.4. Heat Exchangers

In all heat exchangers, the pressure drop, Δp, of every stream is proportional to the square of the mass flow rate:

$$\Delta p = k_p \dot{m}^2 \quad . \tag{18}$$

As a first-order estimate k_p is assumed to be constant and is calculated based on the pressure drop known at design conditions. The heat transfer coefficient k between the hot and the cold fluid is described as linearly dependent to the two mass flow rates by

$$\frac{k}{k_o} = k_m\left(\frac{\dot{m}_1 / \dot{m}_{10} + \dot{m}_2 / \dot{m}_{20}}{2}\right) + (1 - k_m) \tag{19}$$

with the dependency factor k_m and k_o as the design value. In this study k_m=1 was used so that the heat transfer coefficient is proportional to the mass flow rates.

4.5. Pumps

In a system like the SEGS plant, many pumps are used for different purposes and in a variety of configurations. Some of them are operated in parallel, others, such as the HTF pumps, are connected in series. Additionally, different operating modes of the pumps such as constant speed or variable speed operation are used.

An example of a complete characterization of a centrifugal pump, including iso-efficiency curves, is shown in the upper diagram of Fig. 6 (Lazarkiewicz et al., 1965). Since no better information was available for the pumps in the system, this was taken as the basis for the calculations.

In Fig. 6 the head H of the pumps is plotted as a function of flow rate Q for speeds varying from $0.5n$ and $1.3n$ and the iso-efficiency curves are eliptical curves with the optimum efficiency[4] of 80% at design conditions (H/H_n=100%, Q/Q_n=100%). The parabolas through the origin represent curves of similar flow conditions. Figure 6 shows how the efficiency of a pump operated at constant design speed can be derived. This is done by plotting the efficiencies found along the constant-speed path for different flow rates, as shown in the lower diagram in Fig. 6.

It is also possible to derive a complete characterization of two variable-speed pumps that are operated in series, where one of those is bypassed until a particular flowrate is achieved (Fig. 7). If two pumps are operated in series, the flow rate through both of them is the same and each pump has to provide half the head necessary to pump the flow through the system. If the system pressure drop is a function to the square of the flow rate, curve A-B-C-D in Fig. 7 then represents the head of one of the two pumps operated in series. If only one pump is used in the system at low flow rates, this pump has to provide the full head, which is represented by curve A-E-F.

The corresponding efficiency curves for the two operating strategies are plotted in the lower diagram in Fig. 7. These show that an optimum efficiency is reached if two pumps are operated in series down to mass flow rates of about 70%. Below that, only one pump should be operated.

In EASY, the thermal efficiency, η_S, of a pump at part load conditions is described as a function of mass flow rate by

$$\frac{\eta_s}{\eta_{so}} = e_{mo} + 2(1-e_{mo})\frac{\dot{m}}{\dot{m}_o} - (1-e_{mo})\left(\frac{\dot{m}}{\dot{m}_o}\right)^2 \qquad (20)$$

with η_{so} as the efficiency of the pump at design conditions, $\dot{m}_o$ as the design mass flow rate and e_{mo} as a parameter defining the shape of the efficiency curve. For constant speed pumps e_{mo}= 0 is a good choice because the calculated efficiency corresponds to the

[4] This optimum efficiency is valid for the special case shown in the diagram. It has to be modified dependent on the pump under consideration (75% as shown in Table 1).

characteristic shown in the lower diagram in Fig. 6 for lower than design mass flow rates. A mean efficiency curve for the two HTF pumps in series can be described by e_{mo} = -0.4. With the parasitic power calculated for the HTF pump at design flow (1.56MWe, Table 2), this leads to Table 5 if constant HTF properties are assumed.

Table 5:Parasitic power consumed by the HTF pump
(e_{mo} = -0.4, $P_{el,0}$=1.56MWe)

Flow [%]	100	75	50	25
Parasitics [MWe]	1.56	0.72	0.30	0.12

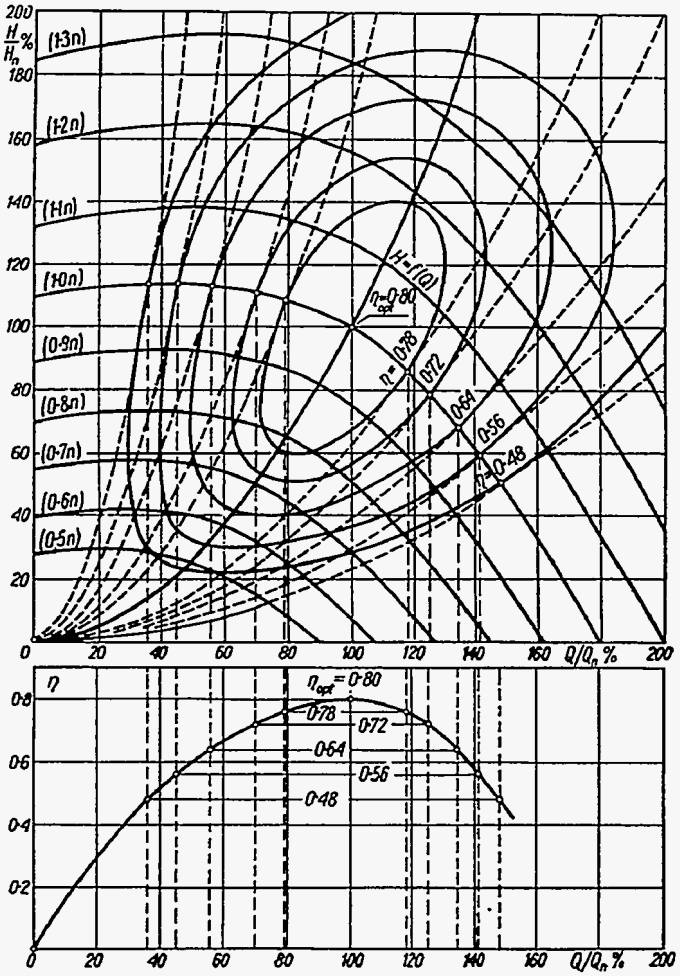

Fig. 6: Complete characterization of a centrifugal pump, including iso-efficiency curves, in a two-dimensional system (Lazarkiewicz et al., 1965).

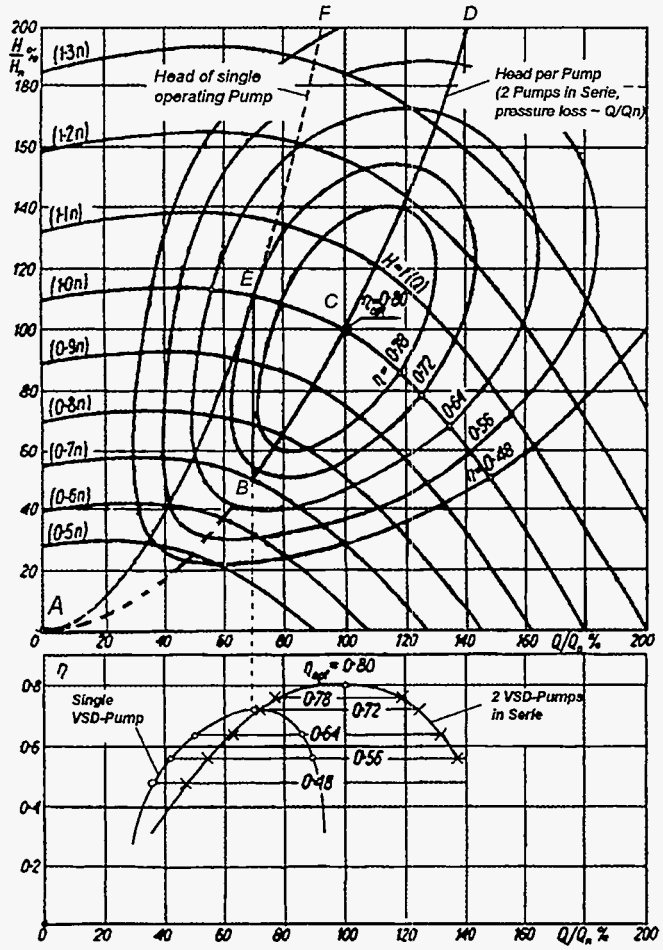

Fig. 7: Characteristics of two centrifugal pumps operated in series.

5. Validation of the Model

In order to validate the model, its results are compared in the following first to the part-load conditions predicted in the technical description (Kearney et al., 1988) and then to the real plant behavior. After that, the energy balances are compared to what SOLERGY predicts in order to evaluate how differences in the model's assumptions influence them. This gives hints for future improvements to the models.

5.1. VP2 and VP3 Solar Operation Mode

The technical description includes ABB predictions for the part load conditions of the Rankine cycle for rated and derated solar and hybrid operation assuming a constant main steam pressure and equality in temperature of main steam and reheat steam. As described in Chapter 2 the pure solar, VP4, mode was used as the design case for this study. Now, as the parameters for the description of the part load conditions of the plant have been defined, it is also possible to compare the EASY results to the predictions of the technical description for the other solar cases.

As the solar field is not included in these calculations, the solar field conditions (mass flow rate and insolation) are predicted by the model to meet the output power. Figures 8 and 9 show the results for the VP3 and VP2 solar-mode as predicted by EASY.

Comparison of EASY results with predictions of the technical description show that the flow conditions and the heat balances are generally close to each other. Nevertheless, there are small differences in the flow rates which are, again, due to the difficulties in defining the LP turbine efficiency for the fourth stage mentioned in Chapter 3. Besides this, the agreement between the two models is good, which means that both models for the Rankine cycle are similar.

5.2. Comparison to Real Plant Operation

Since in a real plant not only transient effects but also changes in the operating strategy play an important role, a comparison of the steady-state EASY model to real plant data is much more complicated. In addition, the solar field conditions are also subject to change and the actual reflectivity of the mirrors throughout the field are only approximately known as are the field locations of HCEs with broken glass envelopes or lost vacuum.

In comparing results to real plant data, it is possible to show how different field conditions affect the results. This study shows how the results compare to the real plant conditions for a summer and a winter day. This allows first the optical performance model and then the heat loss assumptions to be validated, since the latter influence the results much more in the wintertime than on a summer day.

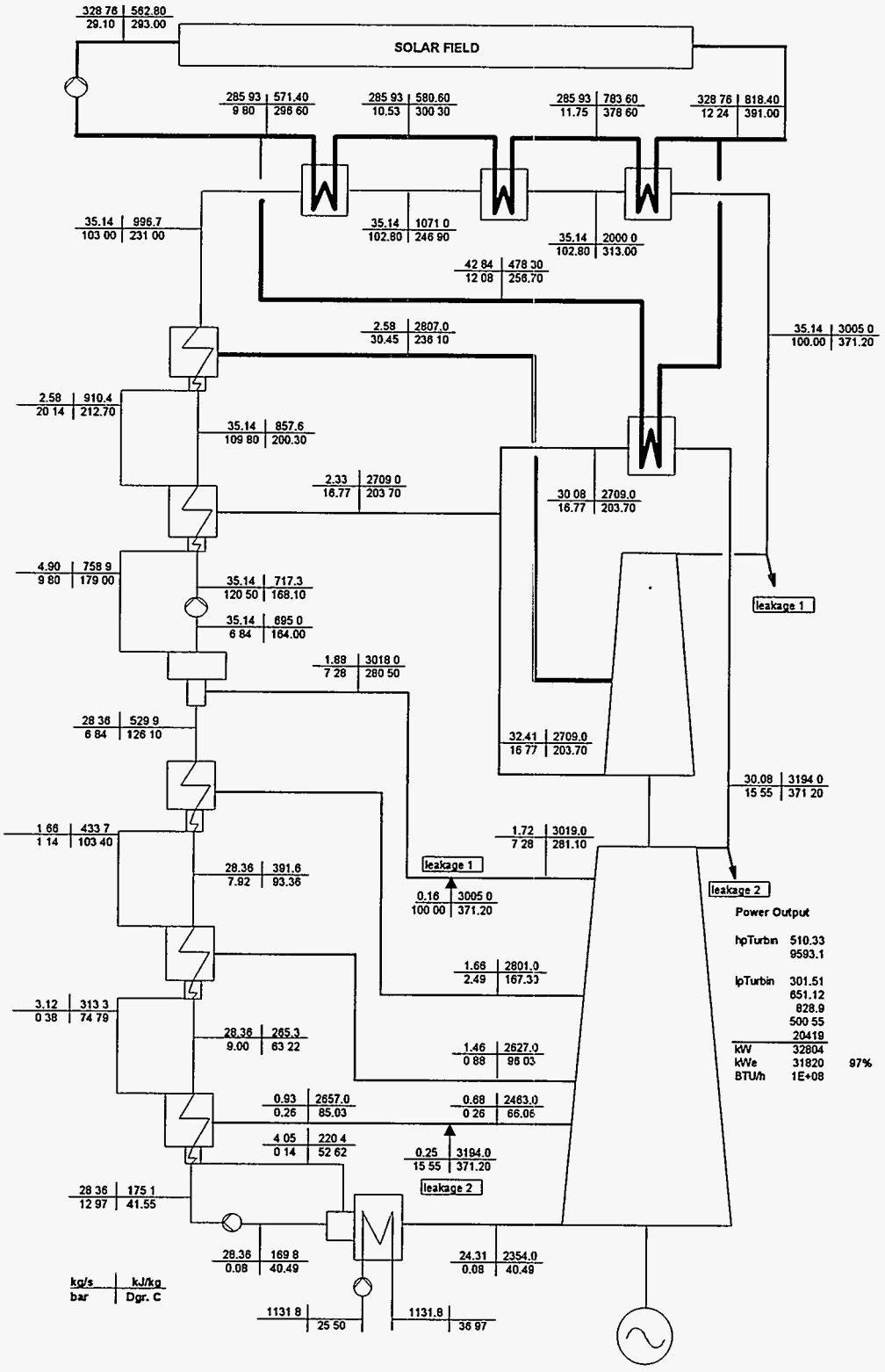

Fig. 8: EASY results for the VP3 Solar-Mode.

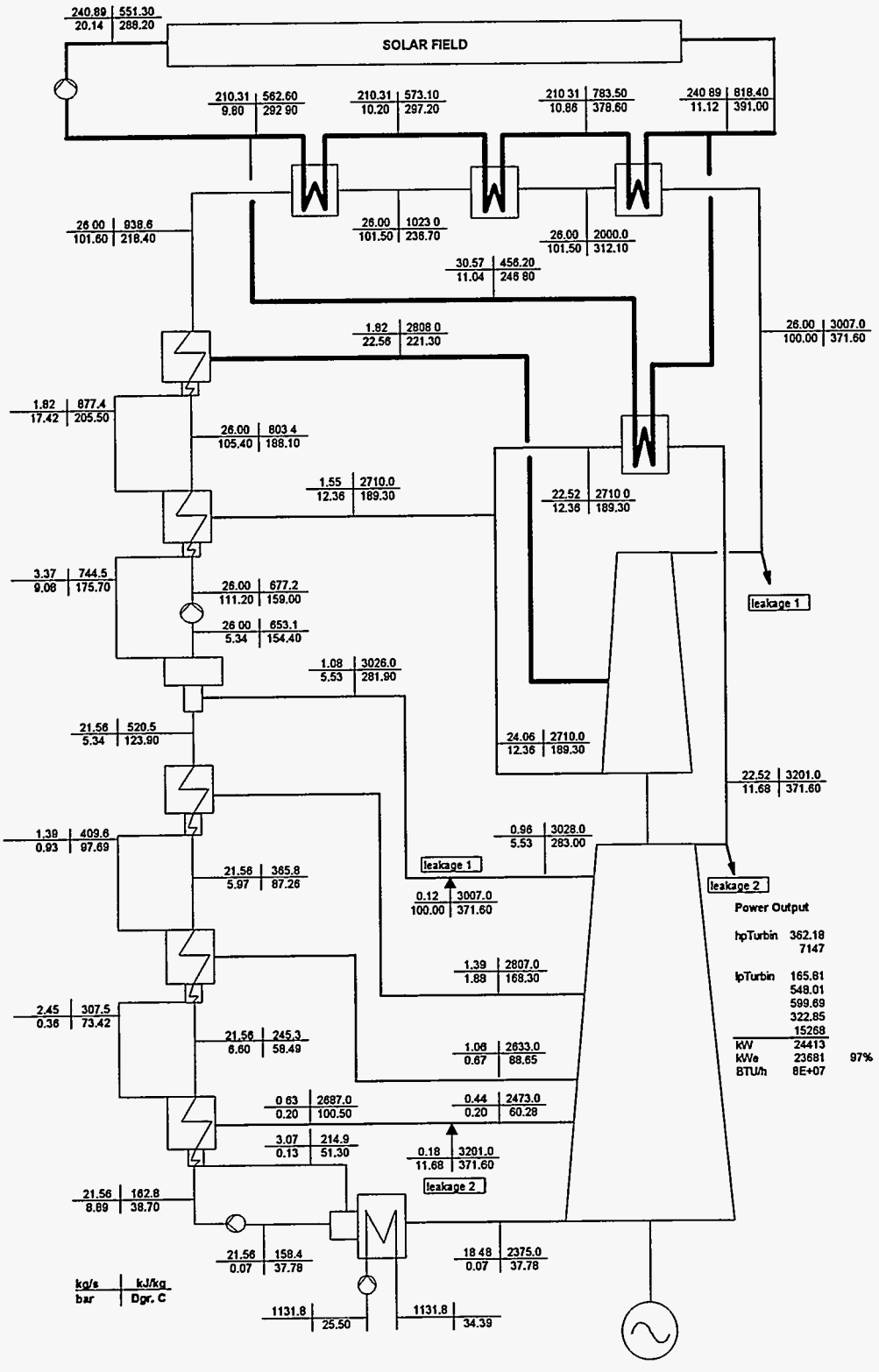

Fig. 9: EASY results for the VP2 Solar-Mode.

5.2.1. Clear Summer Day

Figure 10 shows the insolation conditions and the wind speed measured during a clear summer day. For this day, the plant behavior was predicted with EASY assuming different field conditions as shown in Table 5 and a constant superheating of the main steam in every case. Case S1 functions as the base case for all the calculations. For this prediction, as much information as possible about the solar field conditions for that day were included. The mean reflectivity[5] of the solar field is set to 87.1% and a wind speed of 1m/s (2.2mph) was chosen, which was valid until about 11 a.m. The second case S2 considers a somewhat reduced absorbtivity of all bare tubes due to degradation of the selective coating (Mahoney, 1994). Cases 3-5 are based on this, from which case S3 shows how an additional reduction in the absorbtivity of all receiver tubes influences the result (Mahoney, 1994), S4 shows the effect of increased wind speed, and S5 shows the effect of increasing piping heat losses.

In Fig. 11 the actual, measured gross electric output of the plant is compared with the EASY results. In the EASY calculations, start-up of the plant is not modeled, and no thermal energy is stored in the solar field; this causes the simulation results to be different from the measured data at the beginning and end of the day. No comparison is therefore possible for these times. It can be seen that the model predicts too high an output for all cases but case S3 and that S5 gets close to the actual output.

In comparing the predictions for different wind speeds (cases 1 and 4) with the real plant behavior, it can be seen that the convection losses of bare tubes do not have much influence on the output. On the other hand, this means that generally the optical parameters or the thermal losses of all HCEs or the piping heat losses must be worse than estimated. But here a small change greatly influences the results, as indicated by the differences between cases S2 and S3.

Figures 12 through 15 compare temperatures and pressures predicted by the model for case S3 (for which the predicted gross output is closest to the measured one) with actual plant data. In Fig. 16 the parasitics predicted for the different cases with the actual plant data are shown. Generally a very good agreement between the model and the real plant behavior is found. Major differences only occur for the steam pressures at the inlet of the HP turbine. Here the model predicts about 10 bar more than actually found in the system, which is is not surprising since the model was not fine-tuned to the plant and it seems that the turbine has a higher capacity than assumed in the feasibility study.

---

[5] The optical efficiency has to be scaled by the reflectivity experienced in the solar field compared to the reflectivity assumed for the test collector during the tests. The latter was first assumed to be spray-washed, resulting in a typical cleanliness of 96.3% or a reflectivity of 90.5% achieved after a wash. However, after finishing the calculations, it was found, that the test collector was hand-washed, resulting in a better cleanliness of the mirrors. Assuming that the test collector had a reflectivity of about 93.0% the calculated gross output therefore has to be multiplied by a factor of 97.3%, resulting in a better comparison to the real, measured output.

Table 6: Case definitions for the summer day

Case	HCE/Field Conditions
S1	88.8% with vacuum 2.8% with air 6.2% bare (wind speed 1 m/s=2.2mph.) 1.6% with defective coating 0.6% affected by cooling tower problem (5 SCA o/s) 0.27% of mirrors broken, 100.0 % of SCAs tracking Mirror Reflectivity 87.1%
S2	case S1 with an additional reduced absorbtivity of bare tubes to 75% due to degradation
S3	case S2 with additional "field degradation factor" 95%
S4	case S2 with stronger wind (4m/s=8.8mph)
S5	case S2 with increased piping heat losses (40W/m^2)

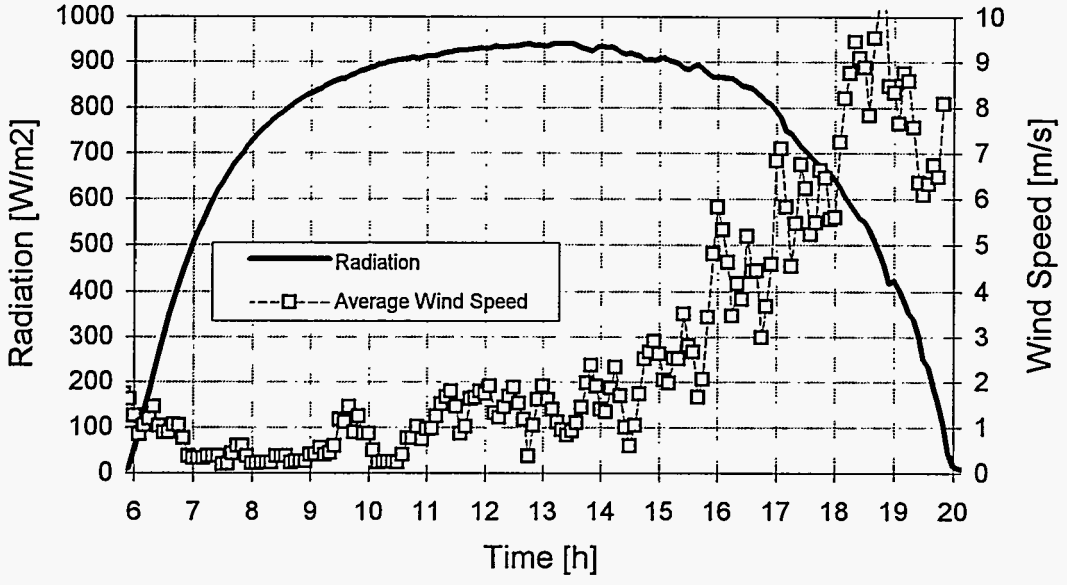

Fig. 10: Insolation and wind speed during a clear summer day.

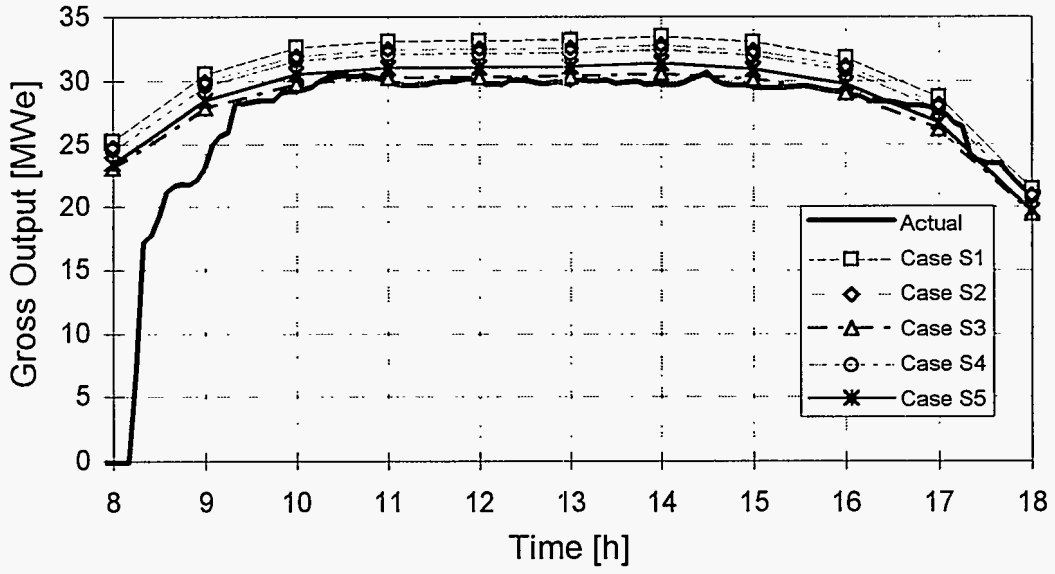

Fig. 11: Actual and predicted gross electric output during a clear summer day.

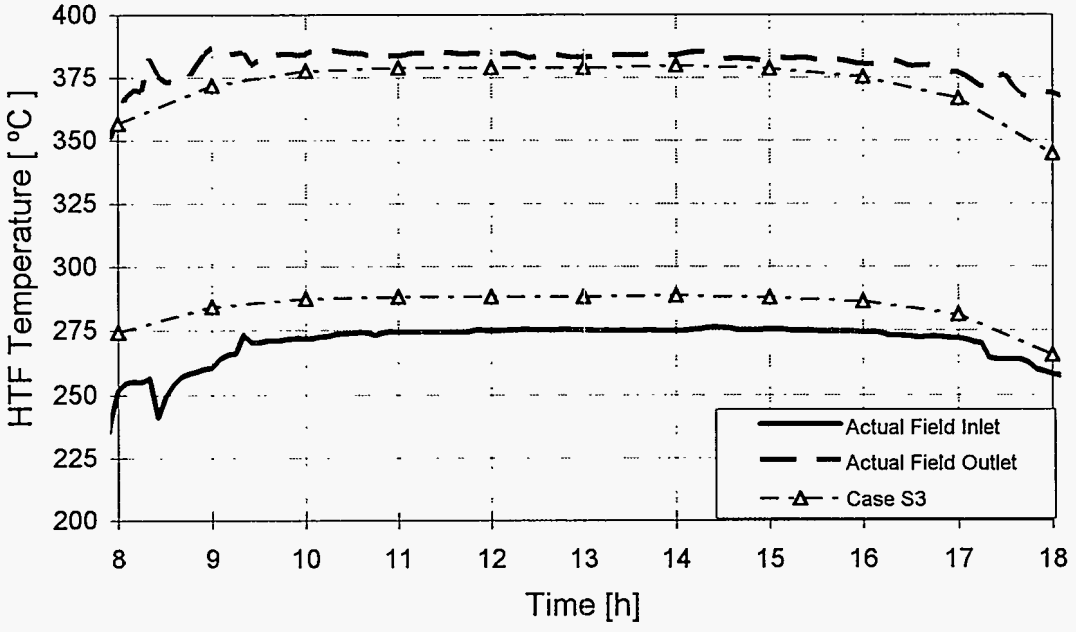

Fig. 12: HTF Temperatures during a clear summer day.

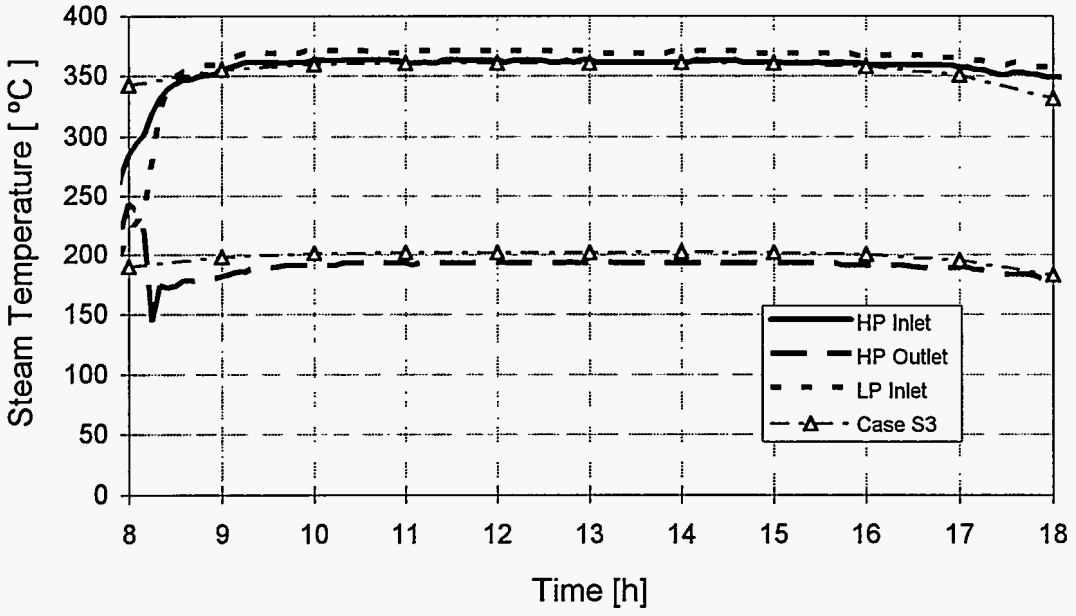

Fig. 13: Actual and predicted steam temperatures during a clear summer day.

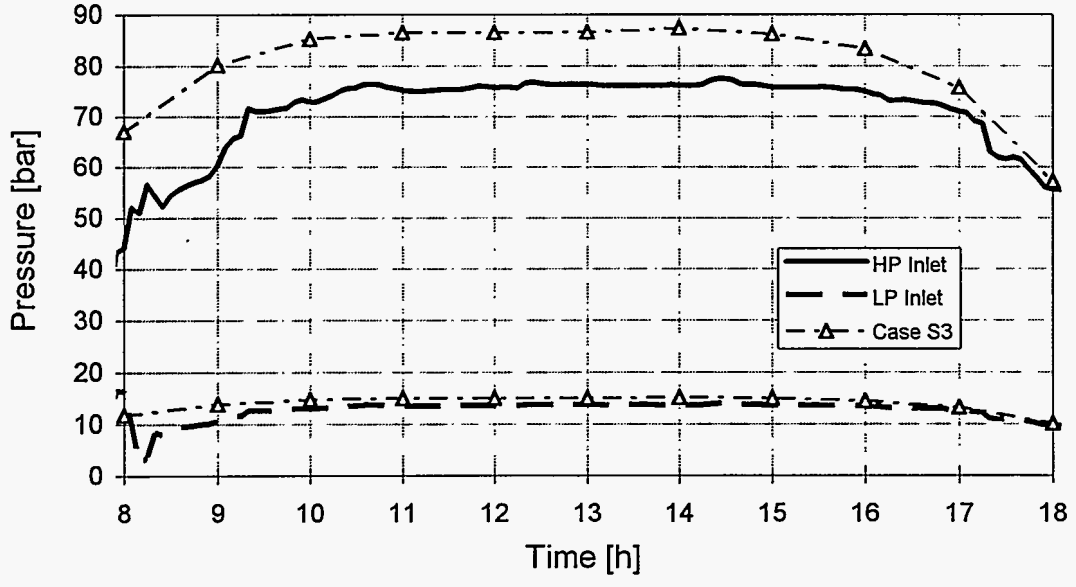

Fig. 14: Actual and predicted steam pressures during a clear summer day.

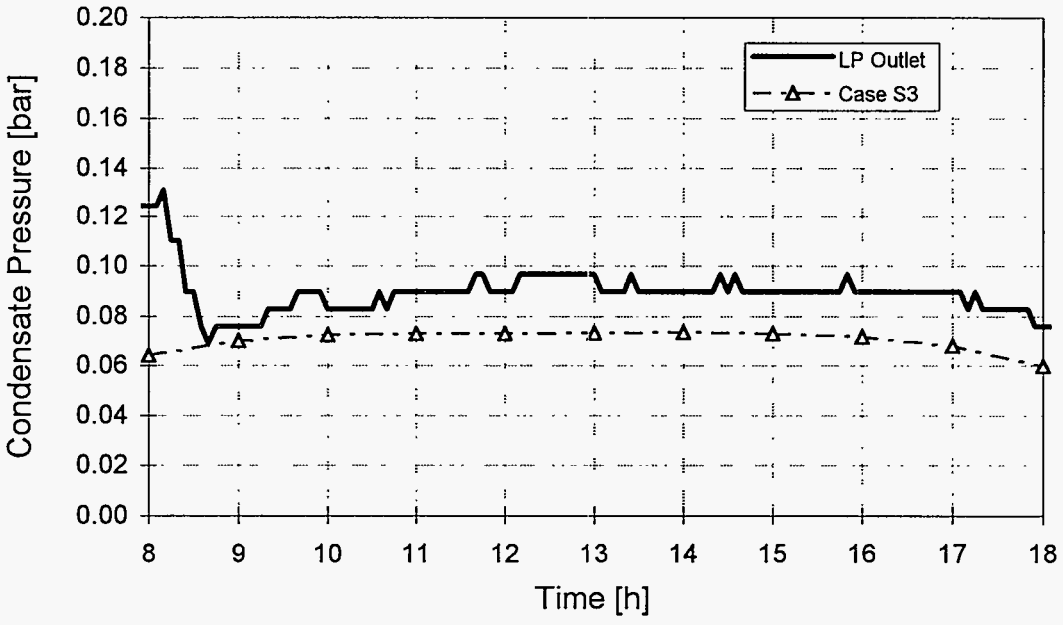

Fig. 15: Actual and predicted condensate back pressures during a clear summer day.

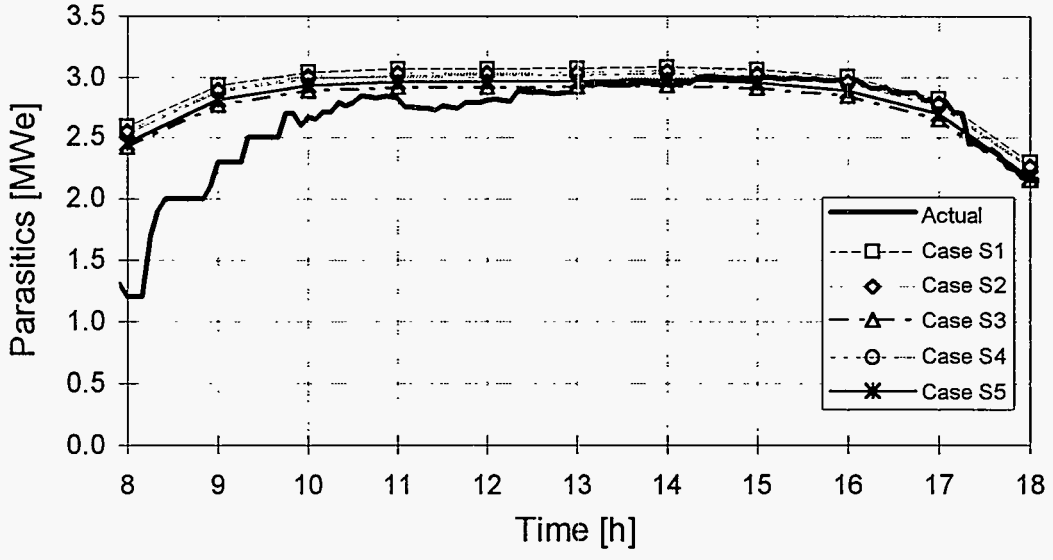

Fig. 16: Actual and predicted parasitics during a clear summer day.

5.2.2. Clear Winter Day

Figure 17 shows the insolation conditions and the wind speed for a winter day. Again calculations were made for this day assuming different solar field conditions, as summarized in Table 6, and a constant superheating of the main steam.

Figure 18 then shows how the gross output predicted by the model for the different cases match the actual measurements. Out of this all predictions can be seen to be too high even at a generally reduced absorbtivity of all HCEs[6] (case W4). A time-shift of about half an hour can be seen between the predictions and the real output due to the time delay of the solar cycle and the heat exchangers.

There are three possible explanations for the high predicted output:

- First, the HCE absorbtivity or the optical efficiency might be lower than for case W4. But this would reduce the output too much for the summer day as shown by case S3 in Fig. 11.
- The second explanation is that the solar field conditions, such as the reflectivity, the number of broken mirrors or the number of bare tubes, are worse than known. But for the winter day, the solar field conditions could be defined more accurately than for the summer day, since better information was available for that period.
- Third, the piping losses, which are assumed to be temperature dependent, are underpredicted by the model (see Chapter 5.3 for the influence of constant piping heat losses on the result for a winter day). Here a more detailed study is necessary to find out the real losses. In the calculations, it was also difficult to define the heat losses of the expansion vessel since its actual condition was not exactly known.

Considering the summer day, a combination of reduced optical efficiency and higher thermal losses might be adequate to represent the real conditions. Comparing the predicted temperatures and pressures for case W3 with the measured data (Figs. 19 through 22), again, temperatures are seen to be close to the actual and HP-Inlet pressure is higher than observed. Finally, the predicted parasitics (Fig. 23) show the same tendency as the gross output and are a little too high.

Table 7: Case Definitions for a Winter Day

Case	HCE/Field Conditions
W1	87.3% with vacuum, 3.0% with air, 7.5% bare (wind 1 m/s=2.2mph), 1.6% with defective coating, 0.6% affected by cooling tower problem (5 SCA o/s) 0.34% of mirrors broken, 100.0 % of SCAs tracking, Reflectivity 90.5%
W2	additional assumption that absorbtivity of bare tubes is reduced to 75% (degradation)
W3	stronger wind (2m/s=4.4mph)
W4	same as case W3 with additional field degradation factor of 95%
W10	same as case W3 with increased piping heat losses of (40W/m^2)

[6] As noted in footnote 5 on page 20, the results should be scaled by 97.3%. Considering that, case W4 represents the actual conditions best. Considering higher piping losses, the results then will be close to the actual, measured output

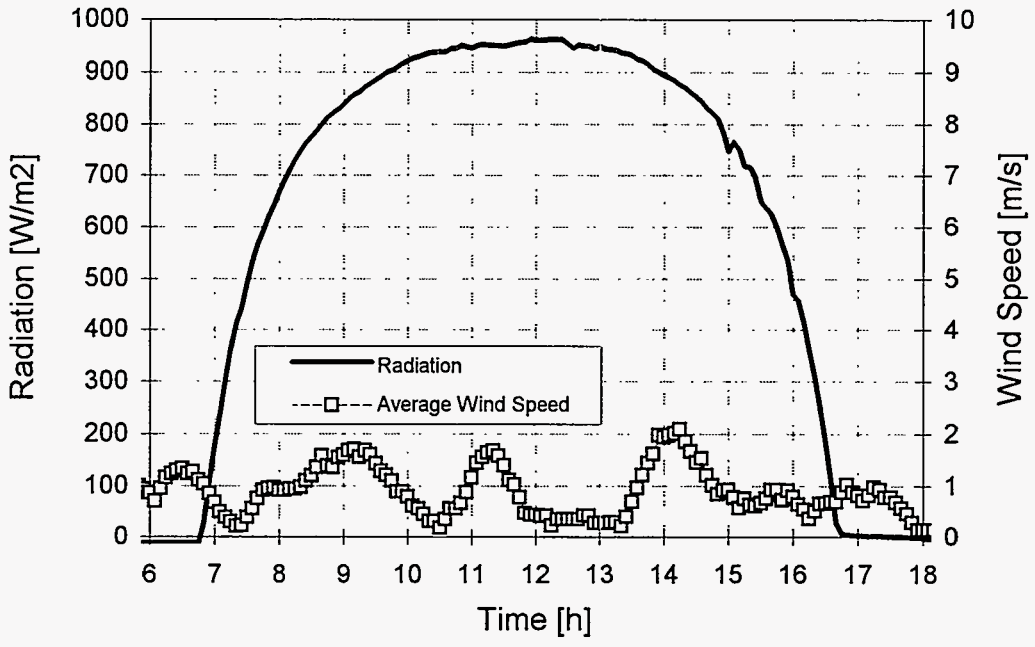

Fig. 17: Insolation and Wind Speed during a clear winter day.

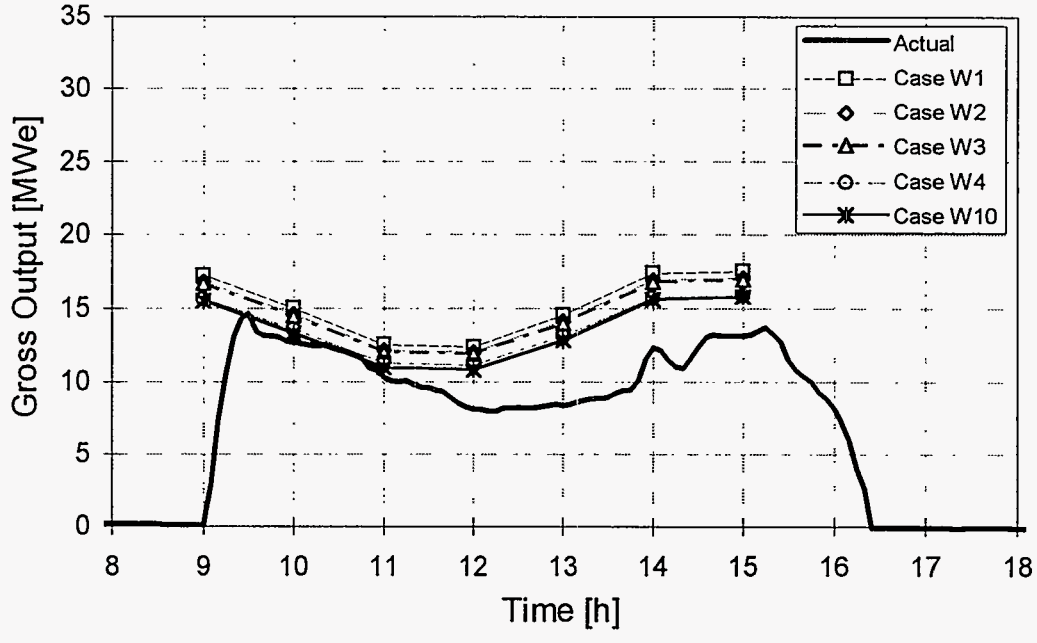

Fig. 18: Actual and predicted gross electric output during a clear winter day.

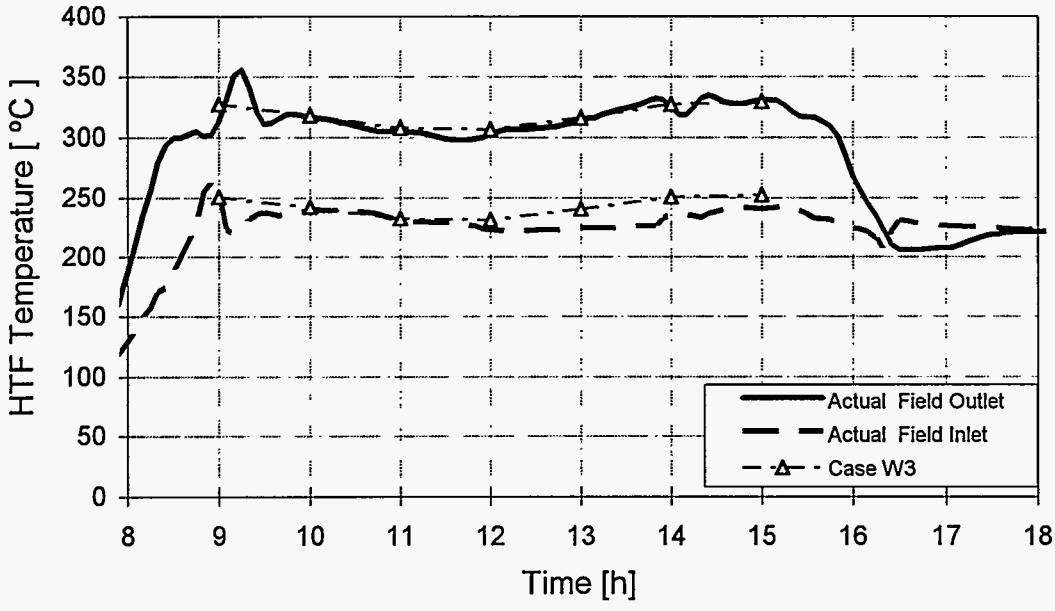

Fig. 19: HTF Temperatures during a clear winter day.

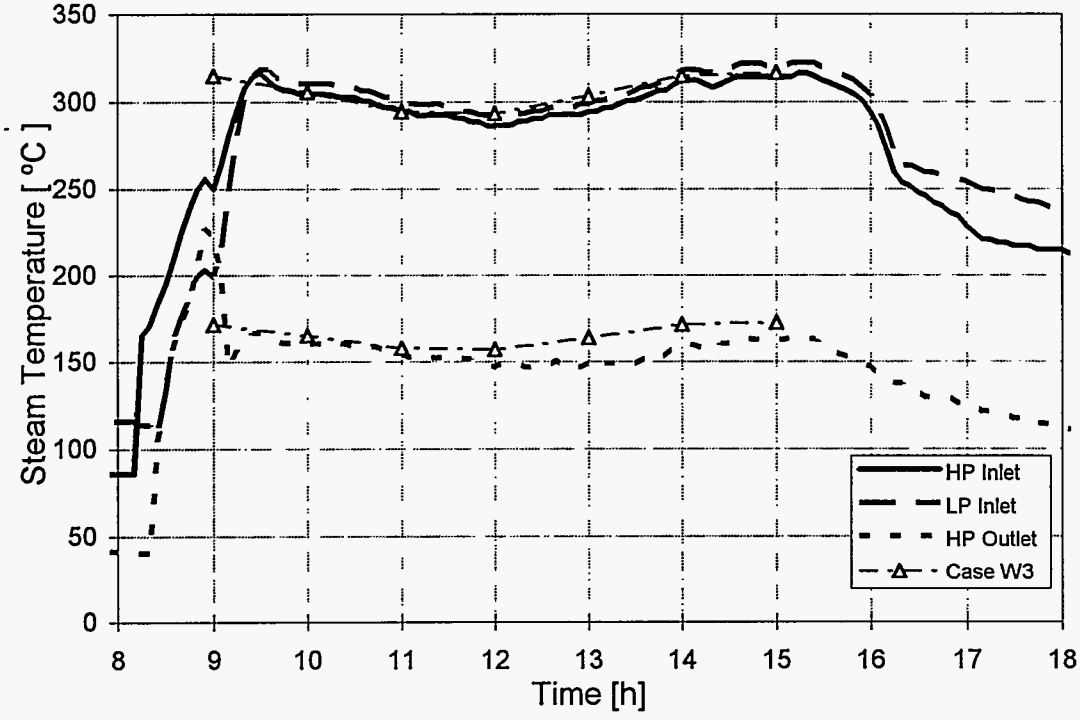

Fig. 20: Actual and predicted steam temperatures during a clear winter day.

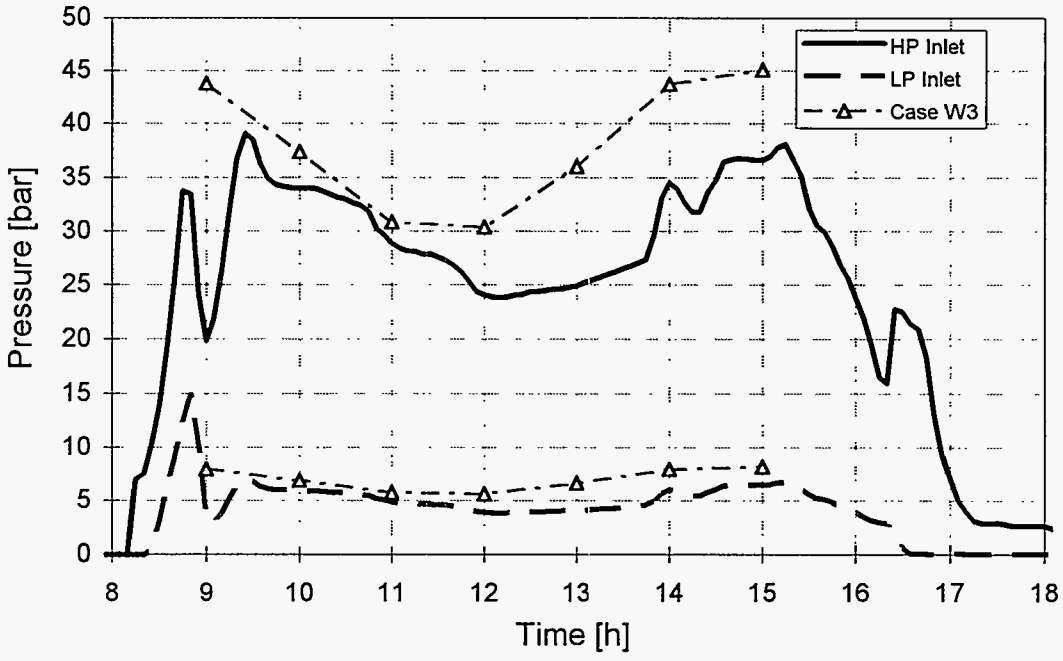

Fig. 21: Actual and predicted pressures during a clear winter day.

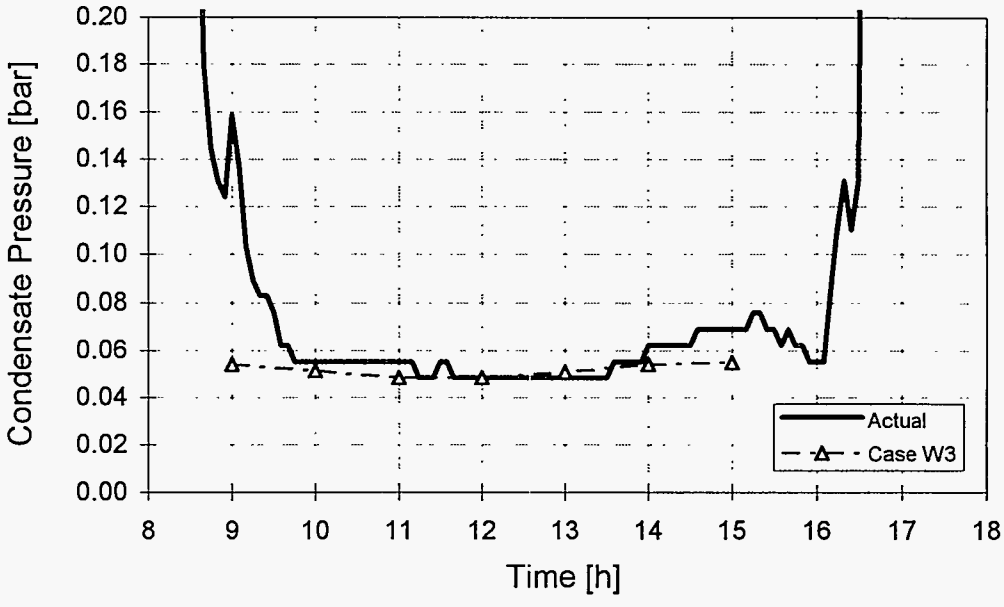

Fig. 22: Actual and predicted condensate back pressures during a clear winter day.

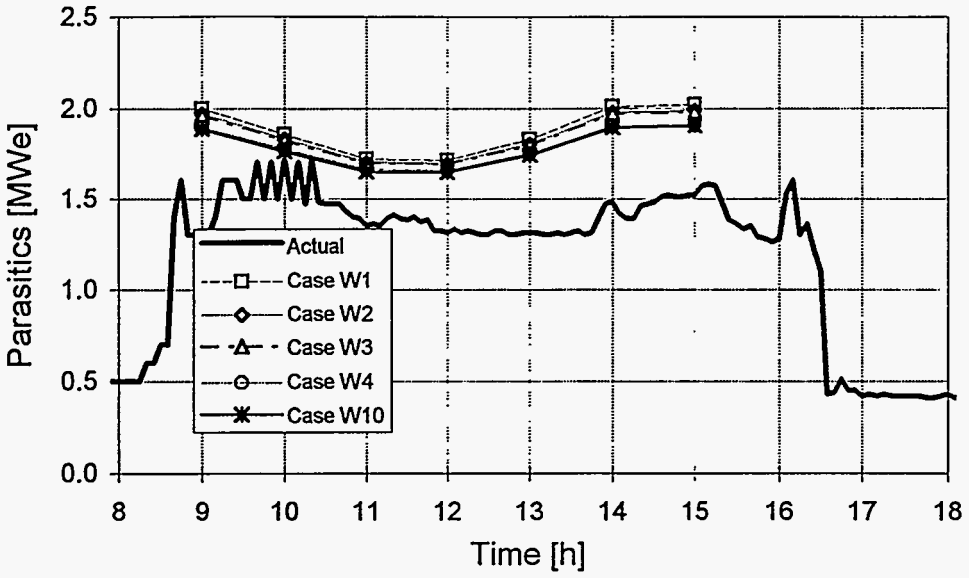

Fig. 23: Actual and predicted parasitics during a clear summer day.

5.3. Comparison with SOLERGY-Results

By comparing the EASY results with the SOLERGY model, the influences of the different assumptions used in the two models can be seen. It is also possible to show clearly how the results are affected by changes in the operating conditions. In SOLERGY, in which only energy balances are used for the calculations, it is assumed that the heat losses of the solar field and all the piping are constant for all loads. For the solar field, 20MWth was used in the calculations based on an estimate of the actual number of broken and low vacuum HCEs for Cermet and black chrome. For the piping 3.7MWth was used.

For comparative purposes, the EASY model was adapted to the SOLERGY parameters so that the solar field losses were the same at design load. To achieve 20MWth in EASY, Cermet for the selective surface and lost vacuum was assumed for all HCEs. For the piping heat losses, a constant value of 3.7MWth was implemented in EASY.

In Fig. 24, the power absorbed by the solar field during a winter day is shown as it is predicted by SOLERGY and with the EASY model for three different operating conditions. The first operating mode considered by the EASY calculations is that the HTF flow rate is held constant at the design value. Second, a constant field outlet temperature is assumed and the third, most realistic assumtion is that the superheating of the main steam is held constant for all loads. The corresponding HTF temperatures at the inlet and outlet of the solar field predicted by EASY for these three cases are shown in Fig. 25.

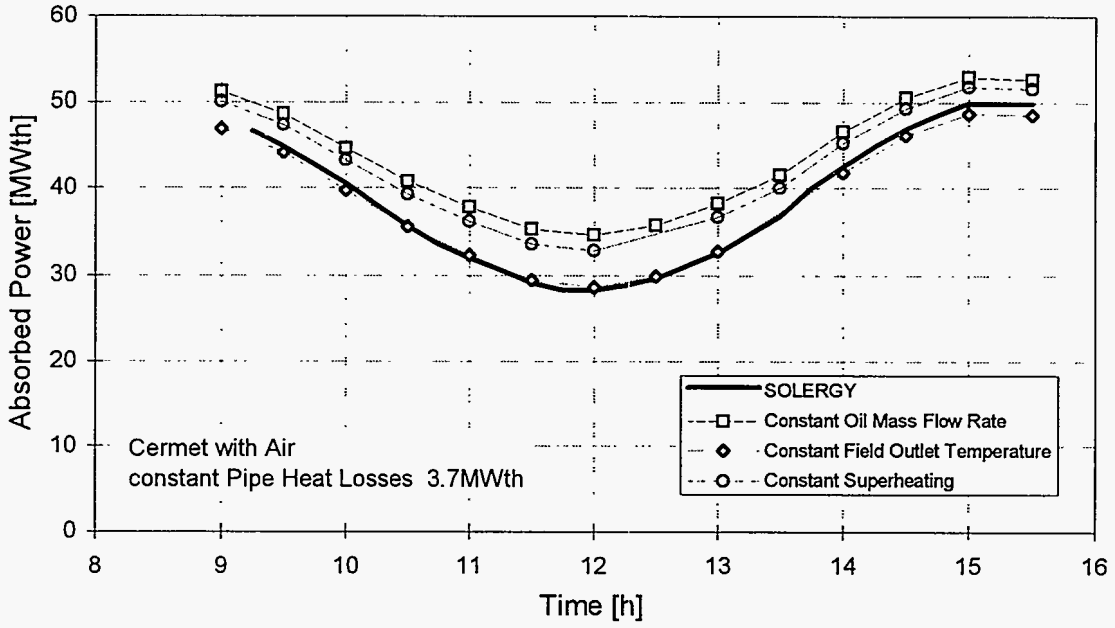

Fig. 24: Absorbed power calculated by SOLERGY and EASY for a winter day.

As can be seen, the power absorbed by the solar field is highly influenced by the operating mode. It decreases with increasing HTF temperatures, which is reasonable since the heat losses of the solar field increase under that condition. For the case with constant design outlet temperature, which is assumed in the SOLERGY model, the EASY results compare well with the SOLERGY results.

The gross output predicted by the two models is shown in Fig. 26. Again, the three different operating modes mentioned above are presented. Now small differences occur between the two models for a constant field outlet temperature, indicating that the Rankine cycle efficiencies are different between the two models. Since the solar field losses calculated with EASY decrease if the outlet temperature decreases, these differences increase at the other two operating modes and the gross output is higher for those cases.

The net output is plotted in Fig. 27. Again the two models are close to each other at constant field outlet temperature. It is also obvious that the differences between the net output predicted for the three operating modes are smaller than for the gross output. This is due to higher parasitics of the HTF pump needed at higher HTF flow rates with lower field outlet temperature. Therefore, the case using a constant HTF flow rate, which shows the highest gross output power (Fig. 24), is, on a net basis, less than on a gross basis. But this changes with the load as can be seen in Fig. 27, where a constant field outlet temperature produces the lowest net output at the lowest load at noon, but at the higher load at morning and evening this is as high as at a constant superheating of the steam.

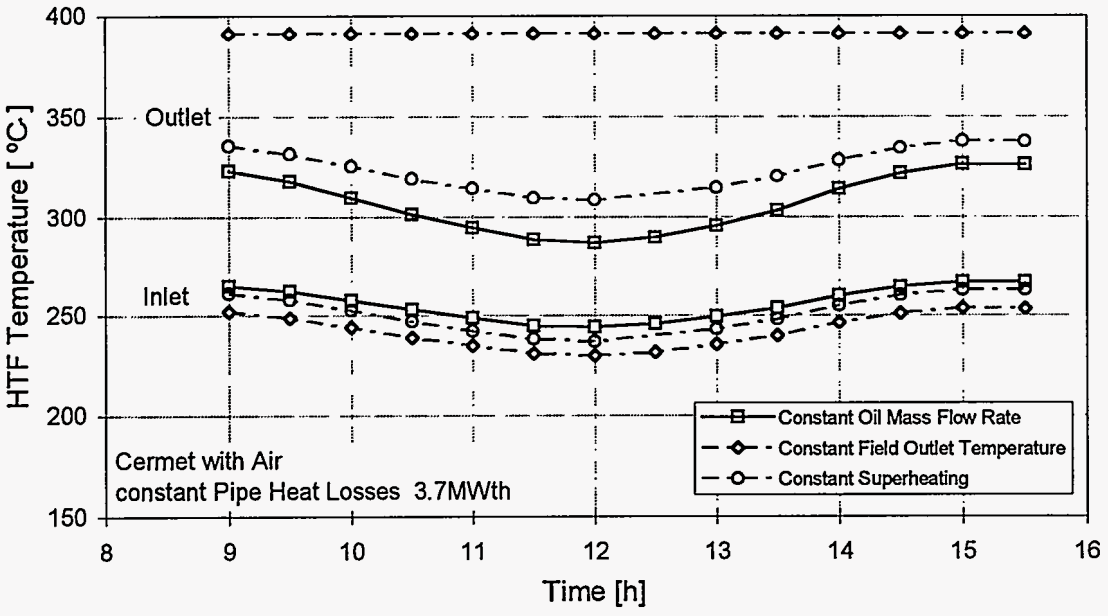

Fig. 25: Solar field inlet and outlet temperatures calculated by EASY for a winter day.

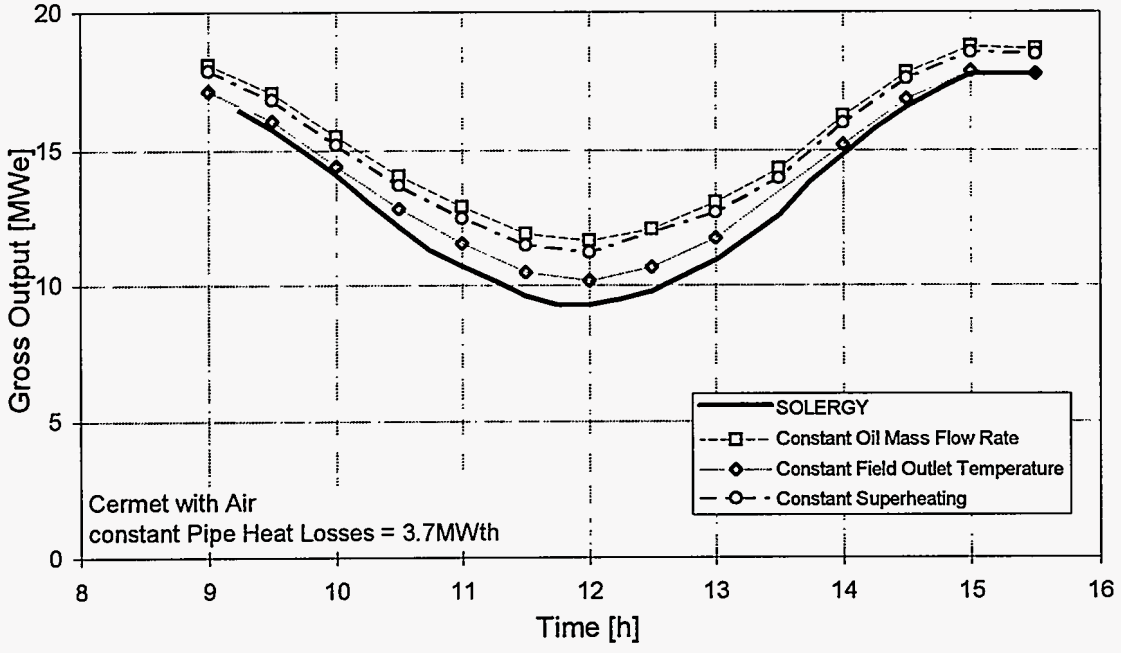

Fig. 26: Gross output calculated by SOLERGY and EASY for a winter day.

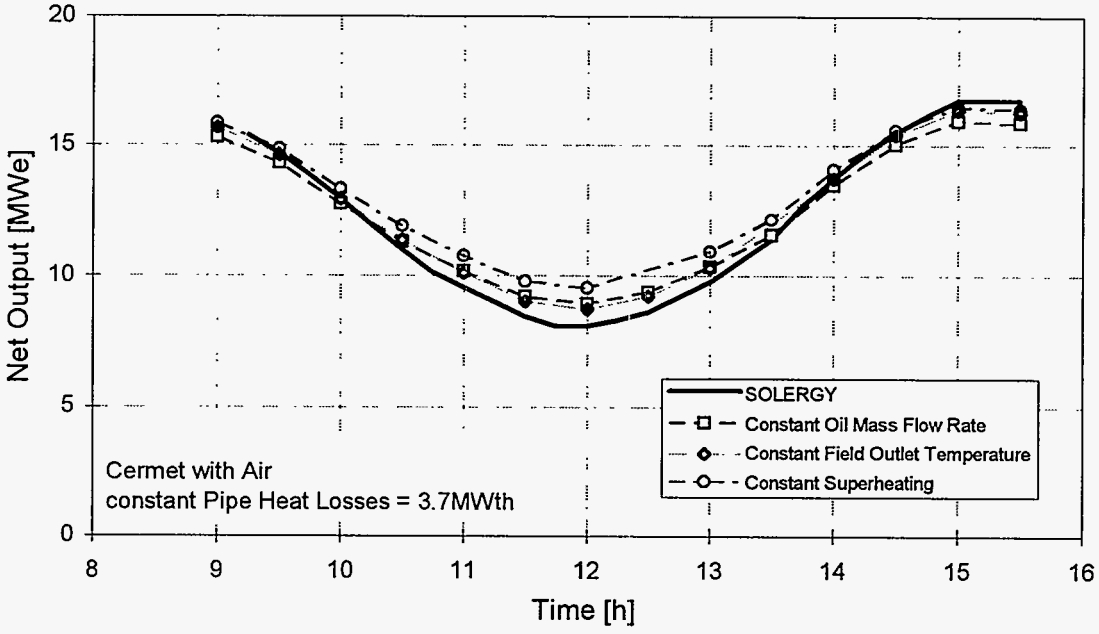

Fig. 27: Net output calculated by SOLERGY and EASY for a winter day.

6. Efficiency Optimization by Changing the Solar Field Outlet Temperature

The following section shows how different operating conditions influence the resulting output of the SEGS plant and how the efficiency can be optimized by changing the solar field outlet temperature. The comparisons are made for three characteristic days - a summer, a winter and a fall day. The same solar field conditions as in Chapter 5 are used for calculations of the summer and winter day; those for the fall day are adopted to the plant conditions found on that.

6.1. Summer Day

Figure 28 shows the gross output of the plant for a summer day. In this, S2 refers to the plant conditions summarized in Table 6. These are also used for cases S6 and S7, where only the operating conditions are changed. In case S6, the superheating of the steam is reduced to 50°C (90°F), in case S7 the solar field outlet temperature is held at its maximum of 391°C (736°F) with superheating temperatures between 65°C (117°F) at noon and 93°C (168°F) at 6 p.m. This compares to 59 °C (106°F) superheating at the design conditions, which is used for case S2.

Obviously, for a summer day, the gross output of the plant is the highest at the lowest superheating temperature of 50°C (90°F), for which the steam quality at the exit of the turbine reaches 90%, and the lowest at the maximum HTF temperature of 391 °C (736°F). Integrating[7] the results over the day - neglecting start-up and shut down times - and comparing the results to each other, the gross output of case S6 is 1.6% higher than predicted for case S2 and 2.6% higher than at the maximum HTF temperature.

The net output of the plant for the three operating conditions is compared in Fig. 29. There, the lower superheating of case S6 is no longer the best, in fact, the net output then is 3.7% lower than at the maximum HTF temperature. The reason for that lies in the high parasitics consumed by the HTF pump in case S6 as shown in Fig. 30, which are probably already beyond its limits. But this is not indicated by the results; the HTF flow rate is predicted to be close to the maximum flow rate of the pumps.

Summarizing the results, it seems that a high solar field outlet temperature always produces the highest net output due to high Rankine cycle efficiencies or, what is more important, low HTF pump parasitics. But the differences, relative to a constant superheating of the main steam of 59 °C (106°F), are smaller at a lower load in the morning and the evening (Fig. 29). But over the day the net output is still 1% higher than in case 2.

[7] A trapezoidal integration method was applied herefore.

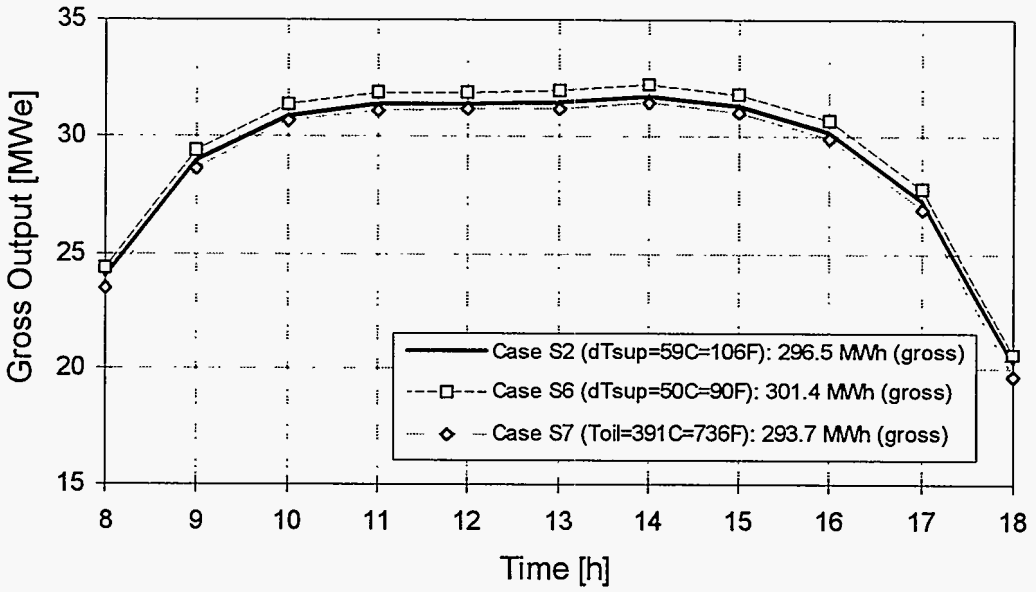

Fig. 28: Gross output for different superheating temperatures on a summer day.

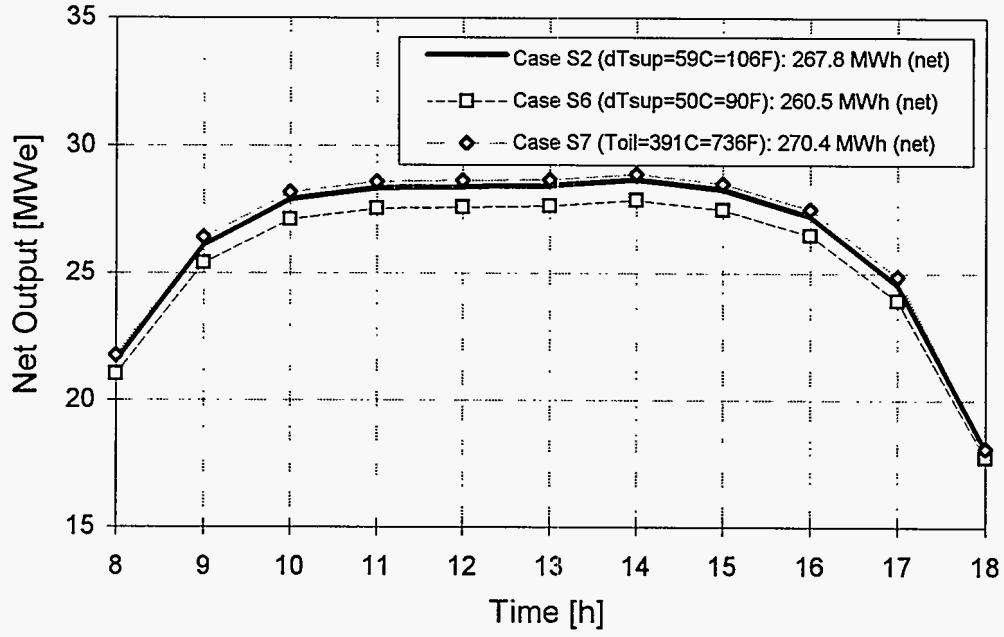

Fig. 29: Net output for different superheating temperatures on a summer day.

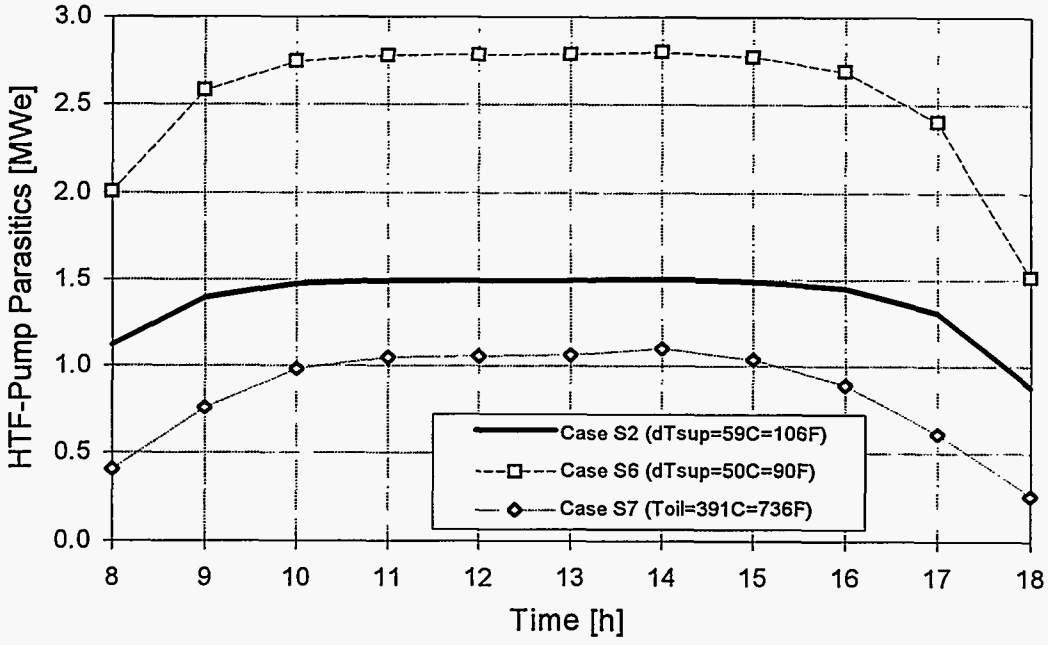

Fig. 30: HTF pump parasitics for different superheating temperatures on a summer day.

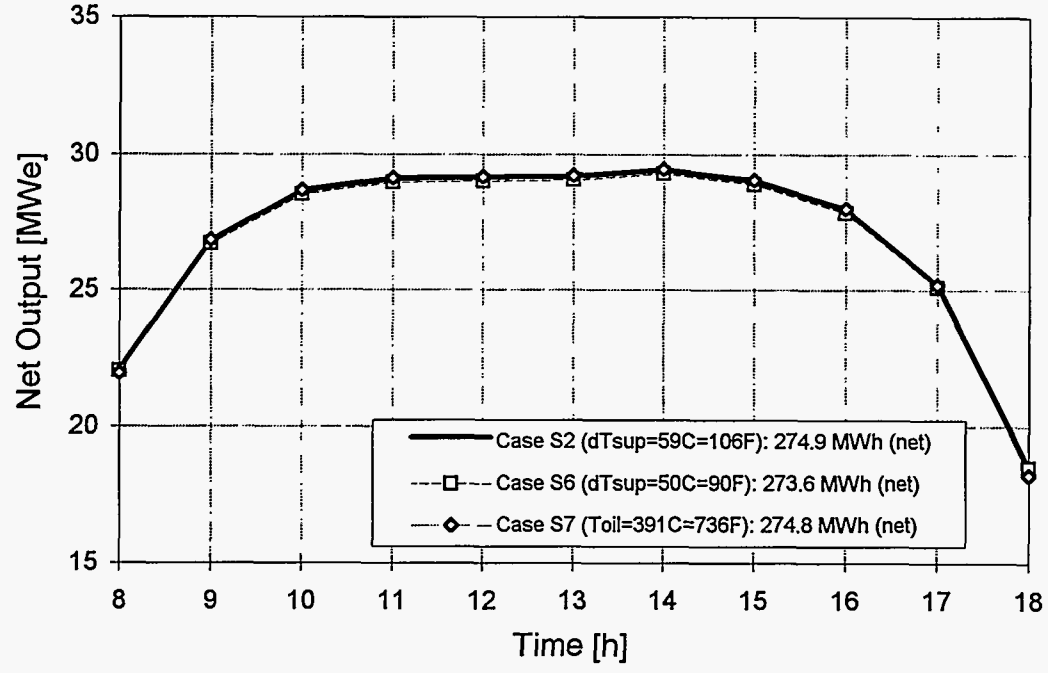

Fig. 31: Net output for different superheating temperatures on a summer day (reduced solar field pressure by 50%).

One change made in the existing plants is that flexible hoses are replaced with ball joints every time a flex hose has to be replaced. The pressure drop in the solar field is predicted to be reduced by approximately 44% after all flex hoses are replaced (KJC Operating Company, 1994). The question then is how this changes the net output at the different operation conditions. As shown in Fig. 31, the differences between the cases are very small under such conditions. Cases S2 and S7 produce nearly the same net output, and case S7 is only 0.5% lower over the day.

6.2. Winter Day

For a sunny winter day, Figs. 32 to 34 show the results for case W2 (dTsup=59 °C=106°F, Table 6), compared with higher and lower superheating temperatures, cases W6-9 and case W5 respectively.. Again, on a gross basis, the plant produces the highest output at the lowest superheating temperature and a decreasing one with increasing superheating of the main steam. On a net basis (Fig. 33) it can be seen that case W2 is the optimum operating mode. It produces a slightly, 0.1% higher net output than case W6, about 0.7% more than case W5, and about 3.4% more than case W9. If the pressure drop in the solar field is reduced this changes so that the operating conditions of case W5 (dTsup=50°C=90°F) produce 0.5% more electricity than case W2 (dTsup=59°C=106°F) and 1.15% more than case W6 (dTsup=67°C=121°F).

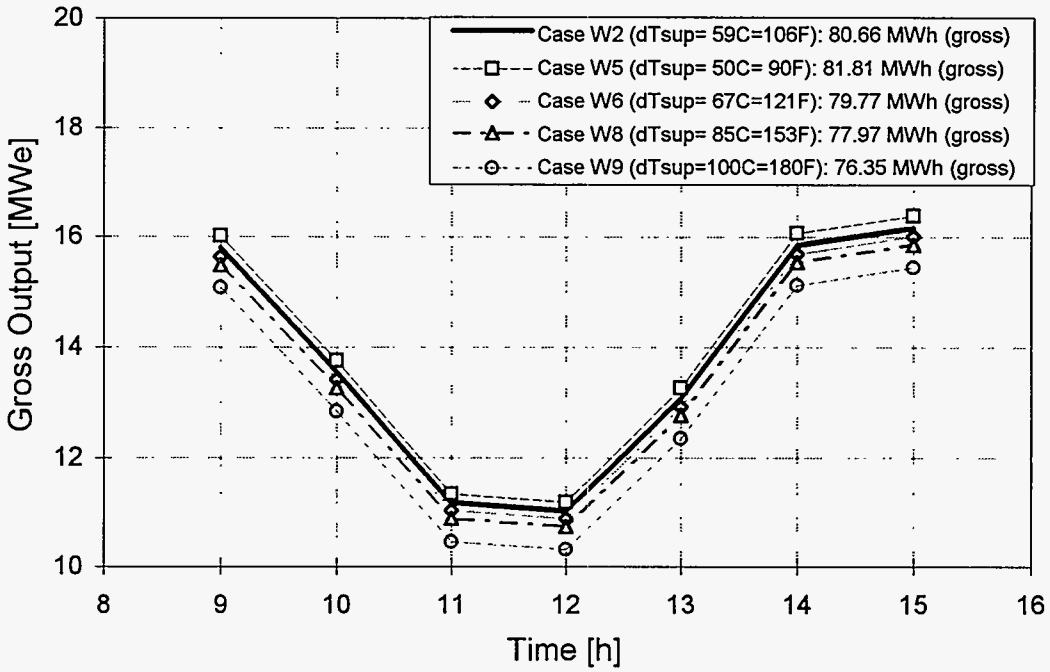

Fig. 32: Gross output for different superheating temperatures on a winter day.

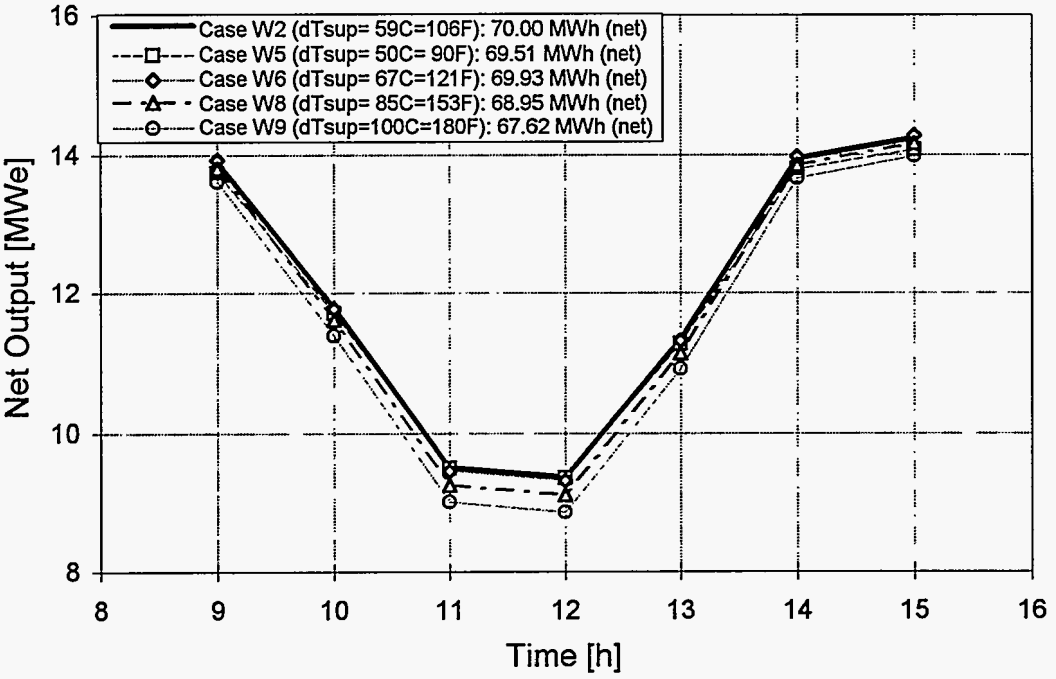

Fig. 33: Net output for different superheating temperatures on a winter day.

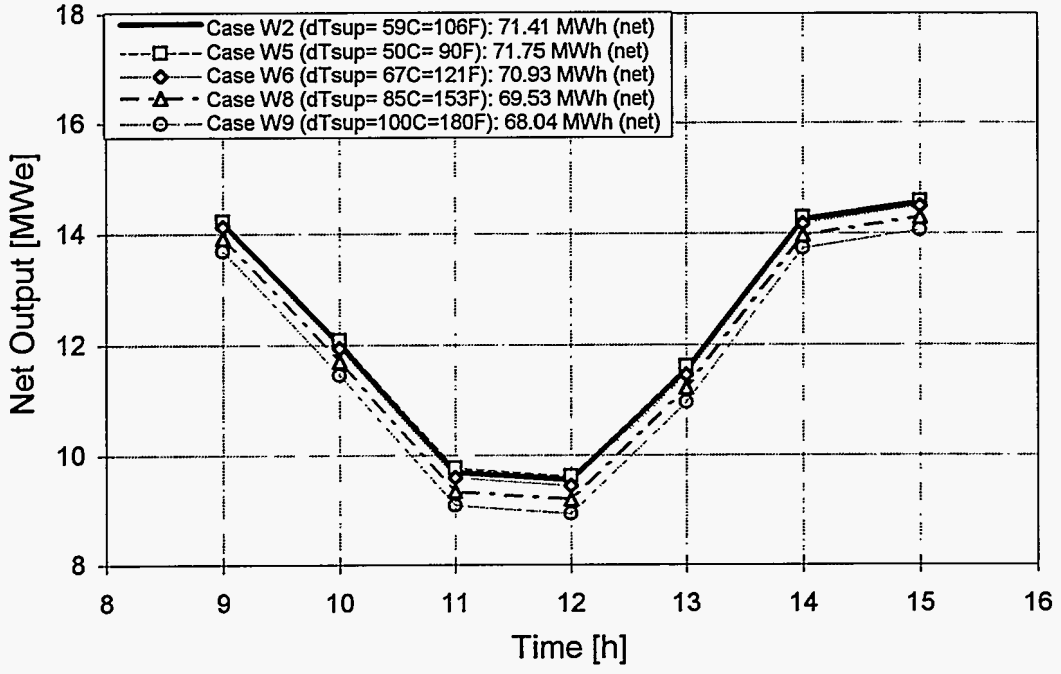

Fig. 34: Net output for different superheating temperatures on a winter day (50% reduced solar field pressure drop).

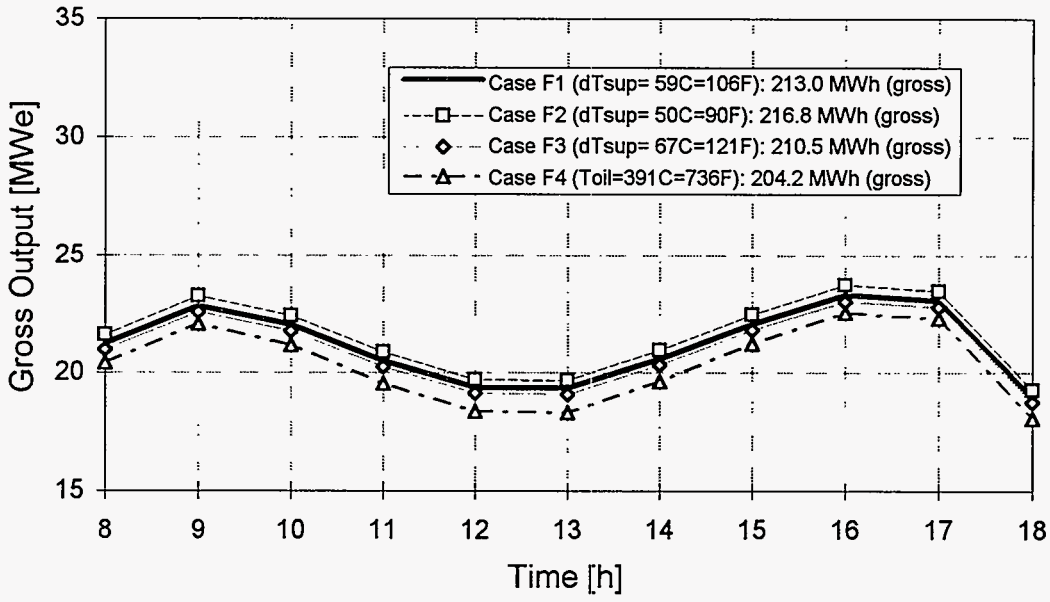

Fig. 35: Gross output for different superheating temperatures on a fall day.

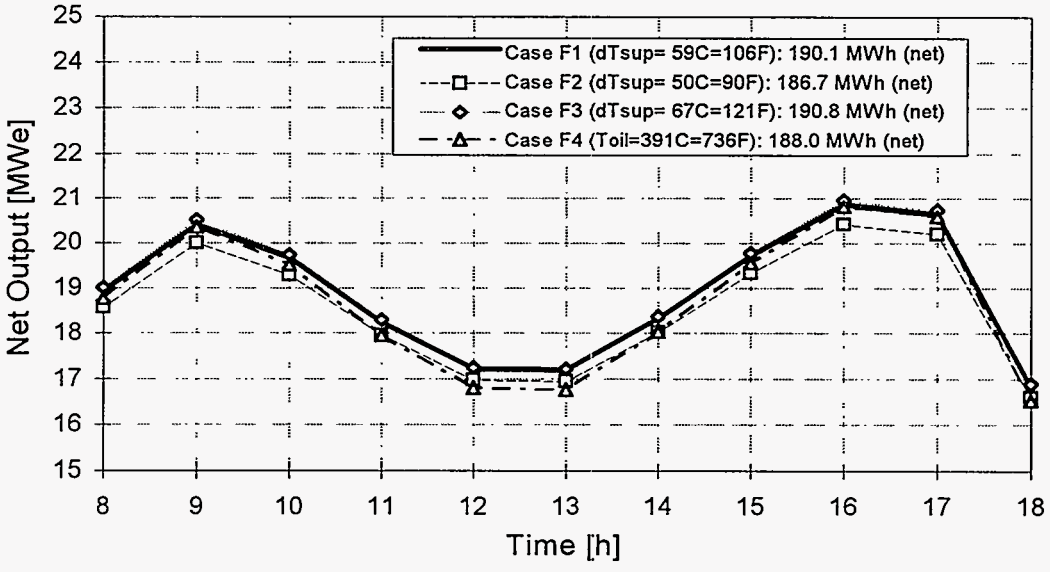

Fig. 36: Net output for different superheating temperatures on a fall day.

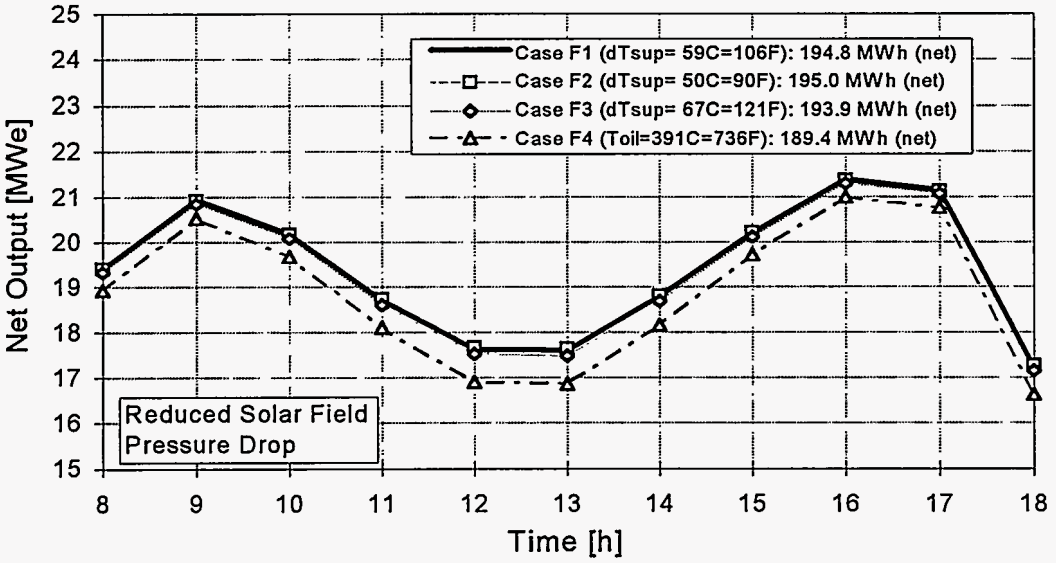

Fig. 37: Net output for different superheating temperatures on a fall day (50% reduced solar field pressure drop).

6.3. Fall Day

For a day in fall, the results show the same tendency as seen before on a gross basis (Fig. 35) but now an optimum superheating temperature (67°C=121°F) with a maximum net output can be found (Fig. 37). This means that for operating conditions in the middle load, the superheating should be increased compared to the design value but should not be chosen as high as possible. At reduced HTF pump parasitics, a small increase in HTF flow rate relative to the design conditions leads to a higher net output.

6.4. Summary

Table 8 summarizes the relative changes of the gross and net output of the plant for the different operating conditions. In all cases, the gross output reaches its' maximum at the lowest solar field outlet temperature, and a strong dependency on the HTF temperature is found. On a net basis it is found that, depending on the time of the year, different superheating temperatures should be chosen. In summer, the highest possible HTF temperature is the best operating mode, but this changes in fall, when it should be decreased somewhat. By doing this, about 1.5% more net electricity could be produced compared to an operation with maximum HTF temperature. But the superheating should still be slightlt increased over the design value. At low load such as on a winter day, it can be seen that the superheating should be chosen at the design value or slightly higher.

In general changes in the operating strategy influence the output more on a summer day than on a winter day, since the parasitics of the HTF pump then are at a higher level. The influence of the parasitics of the HTF pump also becomes clear by looking at the net output predicted for the different operating conditions, assuming a lower pressure drop in the solar field. Then an increase in HTF flow or a decrease of the solar field outlet temperature is favorable most of the year.

As mentioned above, the calculations were made for actual solar field conditions with 6-7% broken HCEs. Therefore, the heat losses are higher than if the plant were in design condition. Estimating the effect of this, one can say that changes in temperature play a minor role if the plant is in good condition, and a higher field outlet temperature then can be chosen. On the other hand, Chapter 5 showed that the heat losses in the model are underestimated compared with the real plant. Therefore the influence of changing the operating conditions could be larger than the comparisons show, and the tendency of having a higher net output would be greater.

Table 8: Relative changes of gross and net output power at different operating conditions

	dTsup [°C] / [°F]		Integrated Gross Output related to maximum	Integrated Net Output related to maximum	Integrated Net Output related to maximum at reduced SF pressure loss
Summer Day	50°C	90°F	**Max.**	-3.66%	-0.47%
	59°C	106°F	-1.63%	-0.96%	**Max.**
	Toil = 391°C / 736°F		-2.55%	**Max.**	-0.36%
Fall Day	50°C	90 °F	**Max.**	-2.1%	**Max.**
	59°C	106°F	-1.75%	-0.37%	-0.10%
	67°C	121°F	-2.91%	**Max.**	-0.56%
	Toil = 391°C / 736 °F		-5.81.%	-1.47%	-2.87%
Winter Day	50°C	90°F	**Max.**	-0.70%	**Max.**
	59°C	106°F	-1.40%	**Max.**	-0.47%
	67°C	121°F	-2.50%	-0.10%	-1.14%
	85°C	153°F	-4.69.%	-1.50%	-3.09%
	100°C	180°F	-6.67%	-3.40%	-5.17.%

7. Summary

In this study, the simulation program EASY is used for detailed thermodynamic calculations of the part-load conditions of a SEGS plant. In the calculations, a solar field performance equation is included that was developed out of measurement results of an LS-2 collector (Dudley et al., 1994). The model results are compared with the real plant behavior for a winter and a summer day and they are also compared with the SOLERGY model. Finally, the code is used to evaluate how different operating conditions, e.g. different solar field outlet temperatures or different main steam superheating temperatures, affect the gross and net output and how this can be maximized at different insolation conditions.

The comparison with the real plant conditions shows that there is still a lack of information concerning actual solar field conditions. It is shown that the effect of wind is predicted by the model to be low. It also seems that the heat losses of the solar field are underestimated since the results are too high on winter and on summer days. Here it is likely that, in particular, the piping heat losses assumed in the calculations were too low. It may also be that the optical efficiency of the solar field was worse than estimated, which is logical, since Sandia's single trough was aligned very well compared with the troughs in the solar field.

When the gross output predicted by the model is close to the actual value, then all the temperatures match the actual plant conditions quite well. For pressures, it is found that these are higher than measured, indicating that the turbine has a higher capacity than assumed.

Comparison with the SOLERGY model shows that at a constant solar field outlet temperature the results are the same for both models. It could also be shown that a reduction of HTF temperature at lower load, which is done at the actual plant, increases the output due to reduced thermal losses of the solar field. To match the actual plant operation varying field and pipe losses should be considered in future SOLERGY calculations.

Finally different operating conditions are shown to affect the output on a summer, fall and winter day. The result for the actual plant conditions is that the gross output always reaches its maximum for the lowest superheating temperature. On a net basis, the high parasitics of the HTF pump change that picture so that the optimum operational strategy depends on the insolation conditions. For a summer day, this optimum operational strategy is to run the plant at the highest allowed HTF temperature of 391°C (736°F). In fall and winter, superheating temperatures slightly above the design value should be chosen, but not as high as possible.

If the solar field pressure drop is reduced by replacing all flex hoses with ball joints, then the optimum operational strategy changes. In this case an increase in HTF flow does not increase the parasitics significantly, so that on a net basis the output is the highest at the lowest possible superheating temperatures in winter and fall. In summer the field outlet

temperature should also be reduced; a constant superheating at the design value is found to be the best here.

Summarizing the results, it can be said that the EASY model agrees well with the real plant conditions but needs to be refined. Some work is also necessary to improve the performance model for the solar field and the thermal loss model for the piping.

8. References

Dudley, V., et al., *Test Results SEGS LS-2 Solar Collector*, SAND 94-1884, Sandia National Laboratories, Albuquerque, NM, 1994.

Flachglas Solartechnik GmbH, *Pre-Feasability Study on a First Solar Thermal Trough Power Plant for Spain*, Prepared for Grupo ENDESA, Madrid, May 1994.

Kearney, D.W., Miller, Ch. E., *SEGS VI - Technical Evaluation of Project Feasability*, submitted to LUZ Solar Partners VI, Jan. 15, 1988.

KJC Operating Company, *O&M Cost Reduction in Solar Thermal Electric Plants - Interim Report on Project Status*, prepared for Sandia National Laboratories, 1994.

Kolb, G., *personel communications*, 1994.

Lazarkiewicz, S., Troskolanski, A.T., *Impeller Pumps*, Pergamon Press, Warsaw, 1965.

LUZ Engineering Corporation, *SEGS VI & VII Operations Manual*, June 15, 1989.

Mahoney, R., *personel conversation*, 1994

Miller, R., *Operation and Maintenance Cost Reduction at Solar Thermal Power Plants*, Proceedings of the 6th International Symposium on Solar Thermal Concentrating Technologies, Sep. 28-Oct. 2, Mojacar, Spain, 1992.

Stoddard, M., Faas, S., Chiang, C., Dirks, J., *SOLERGY - A Computer Code for Calculating the Annual Energy from Central Receiver Power Plants*, SAND86-8060, Sandia National Laboratories, Livermore, CA, May 1987.

Wahl, P., *Object-oriented Design and Implementation of a Software System for Calculating the Part-Load Conditions of Solar Electric Power Plants (in German)*, ZSW-report, SOT-WS 12/92, 1992.

9. Appendix A: Diagrams using English Units

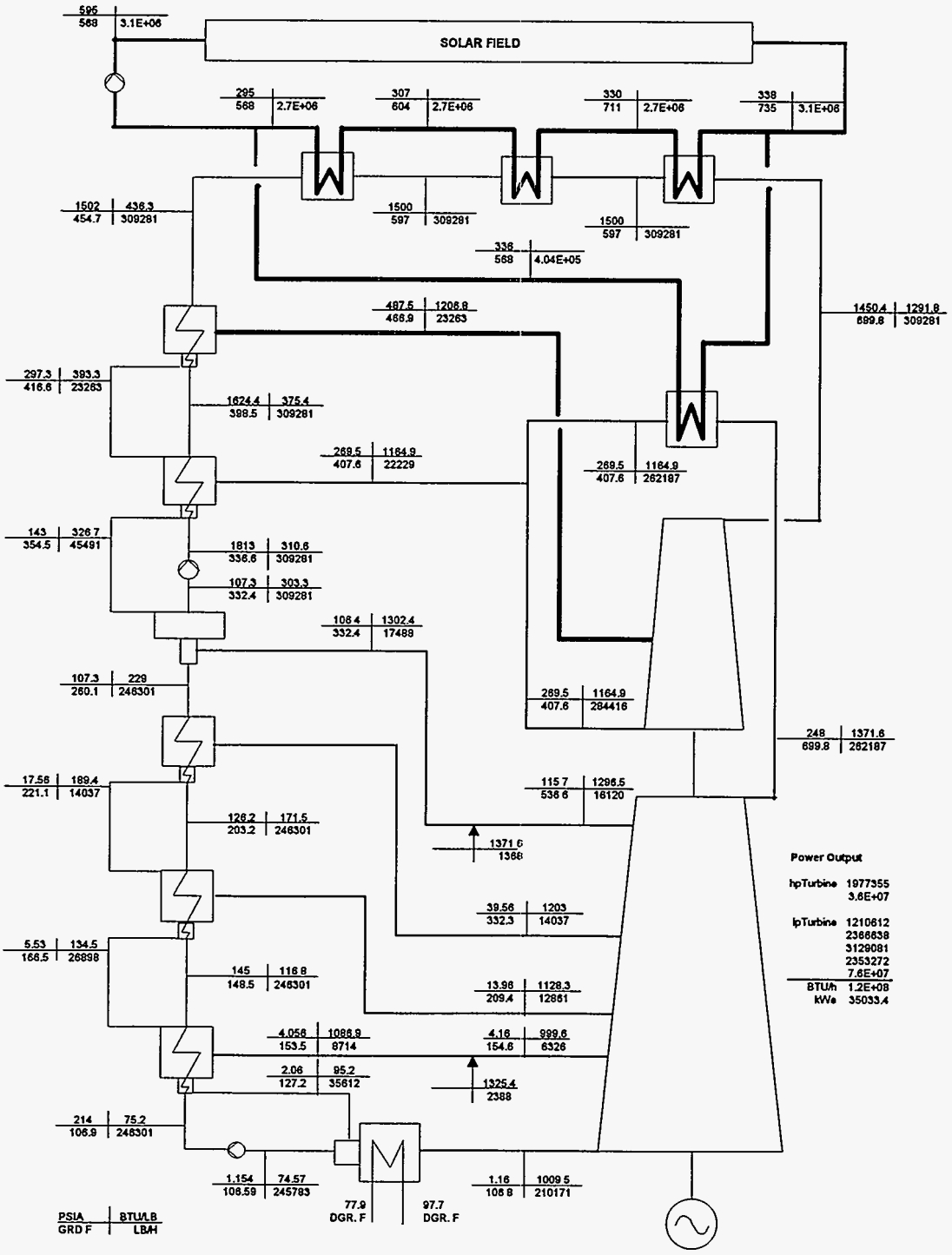

Fig.3b: Design Heat Balances at 100% Solar Load (Kearney et al., 1988)

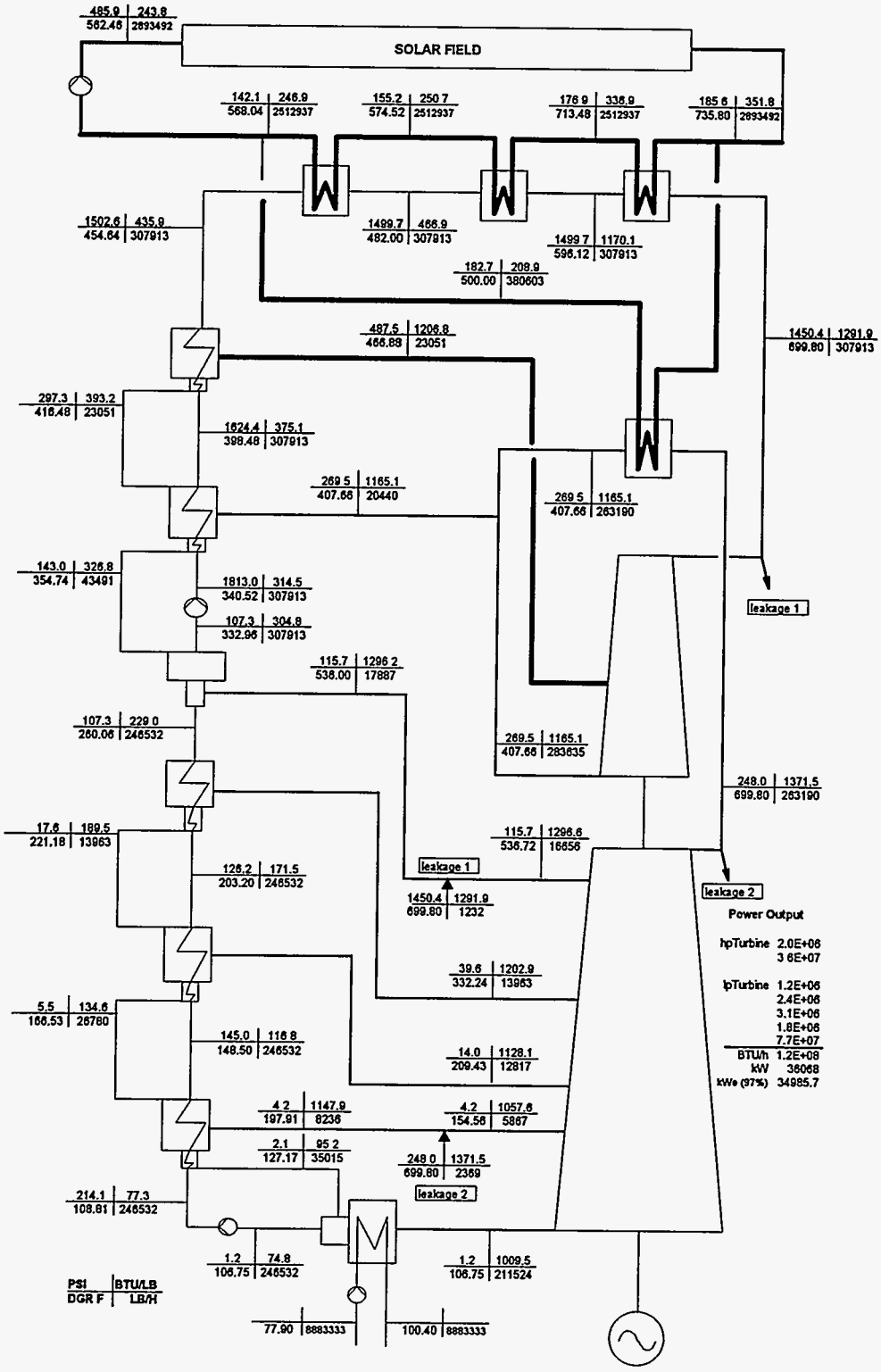

Fig.4b: EASY Results for the Heat Balances at 100% Solar Load.

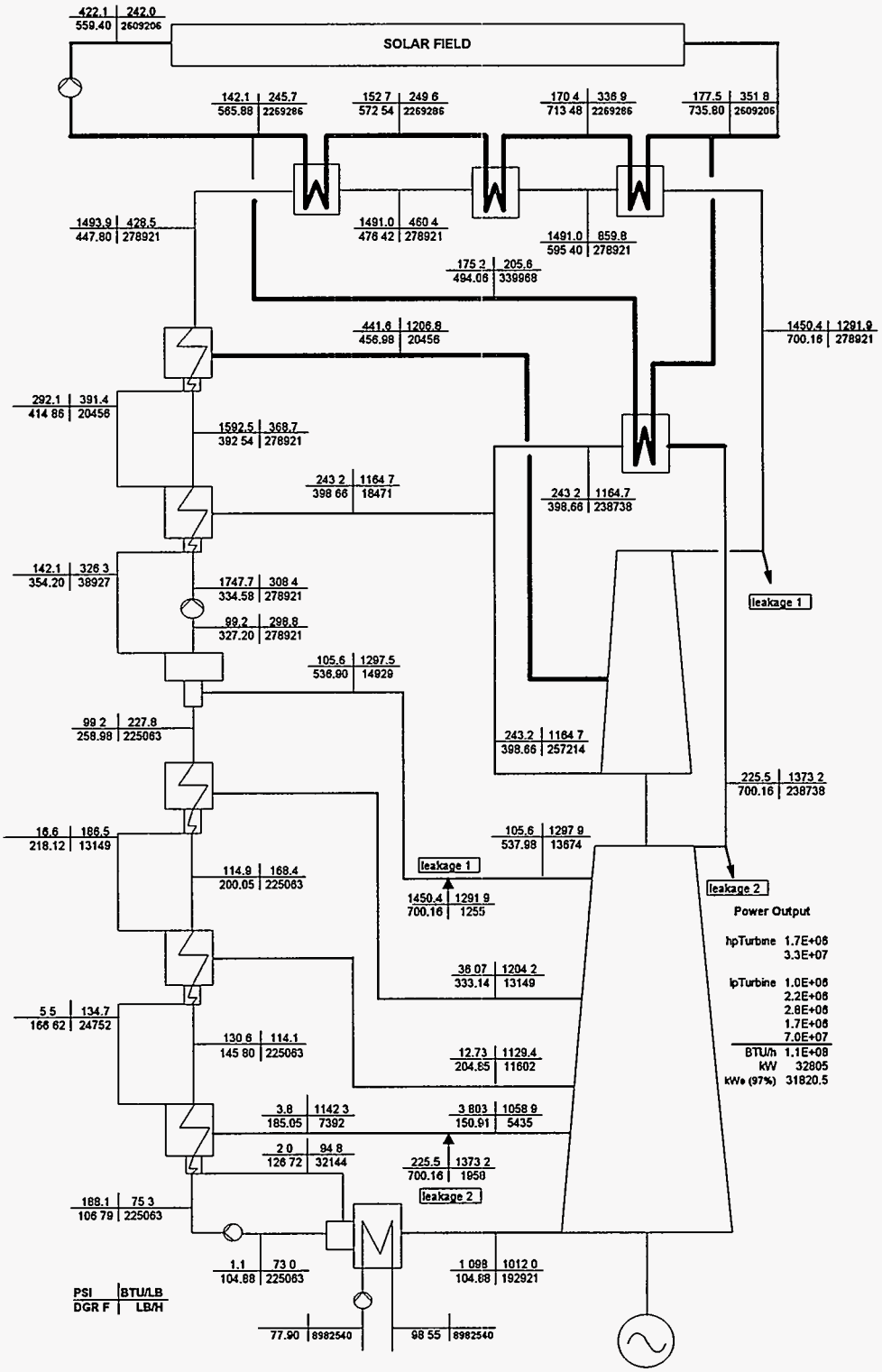

Fig.8b: EASY results for the VP3 Solar-Mode.

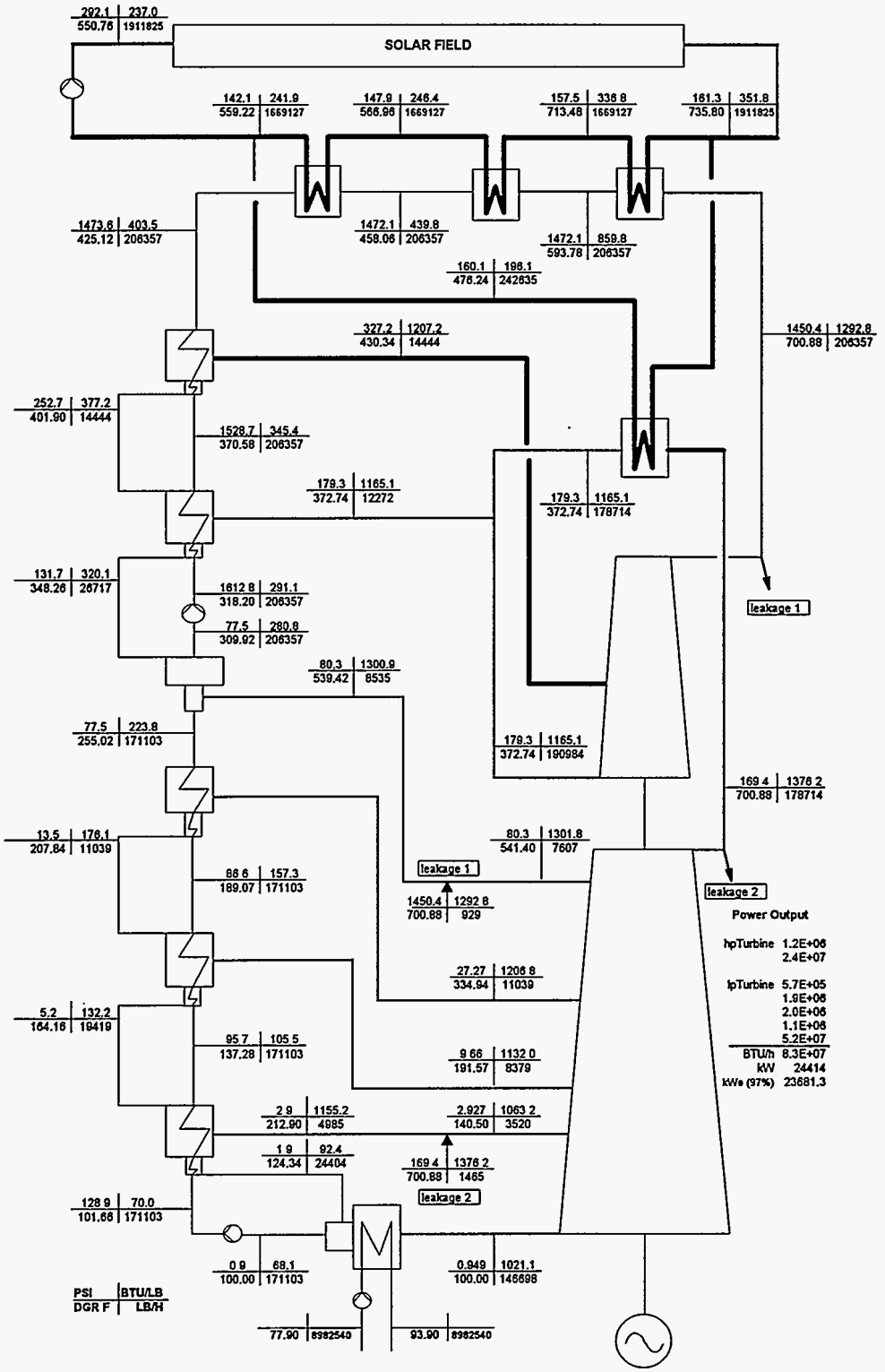

Fig.9b: EASY results for the VP2 Solar-Mode.

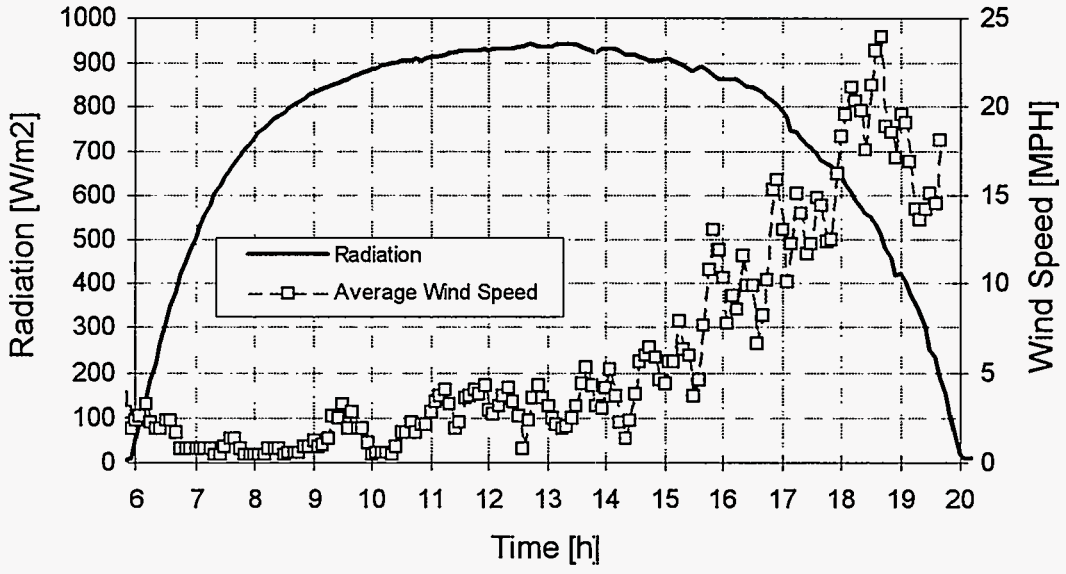

Fig. 10b: Insolation and wind speed during a clear summer day.

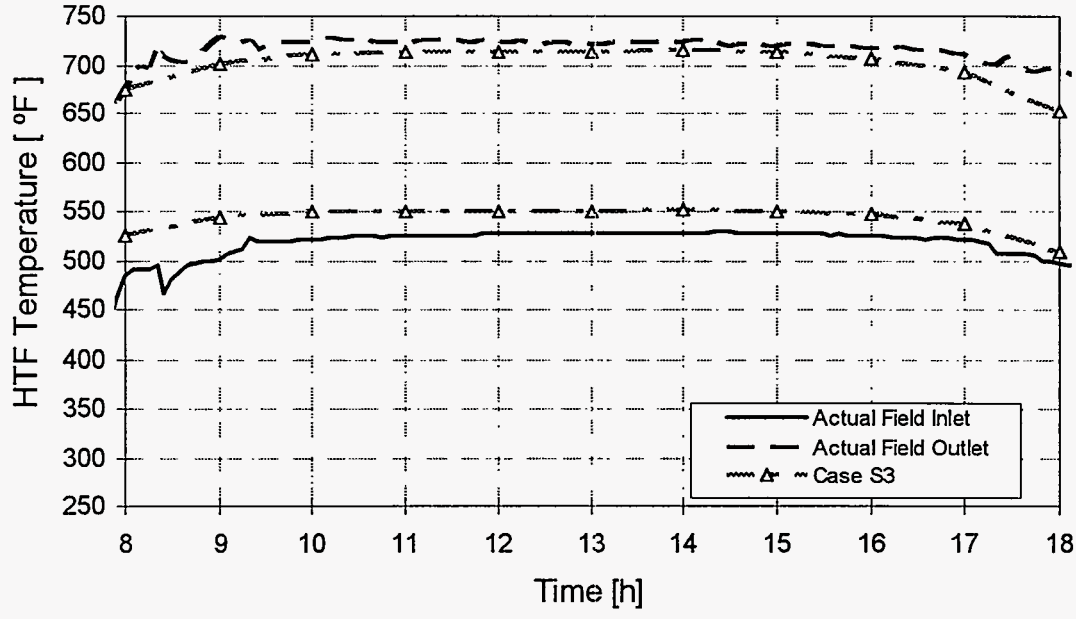

Fig.12b: HTF Temperatures during a clear summer day.

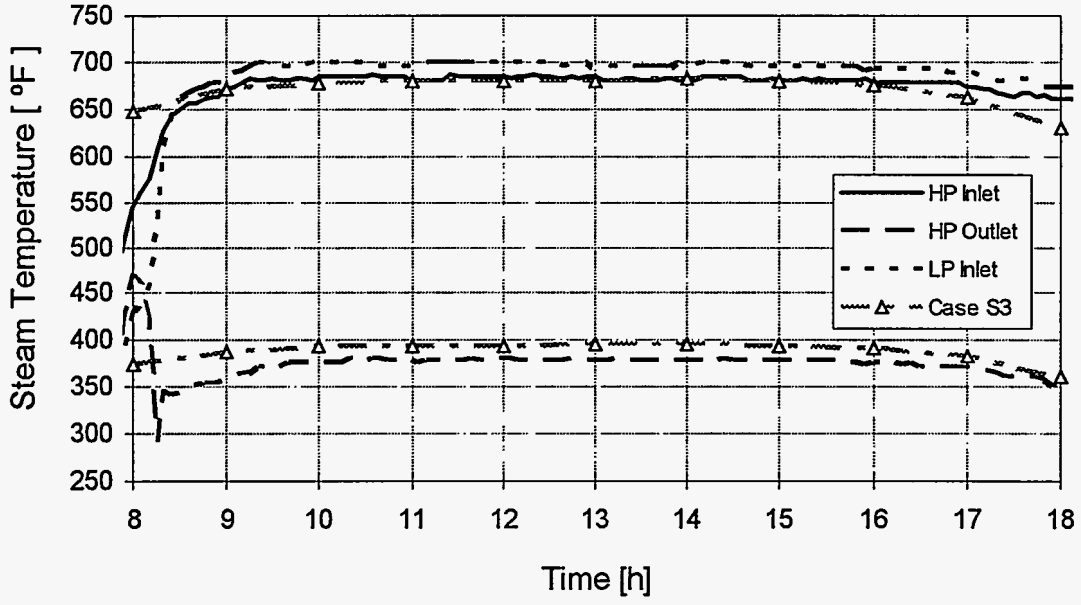

Fig.13b: Actual and predicted steam temperatures during a clear summer day.

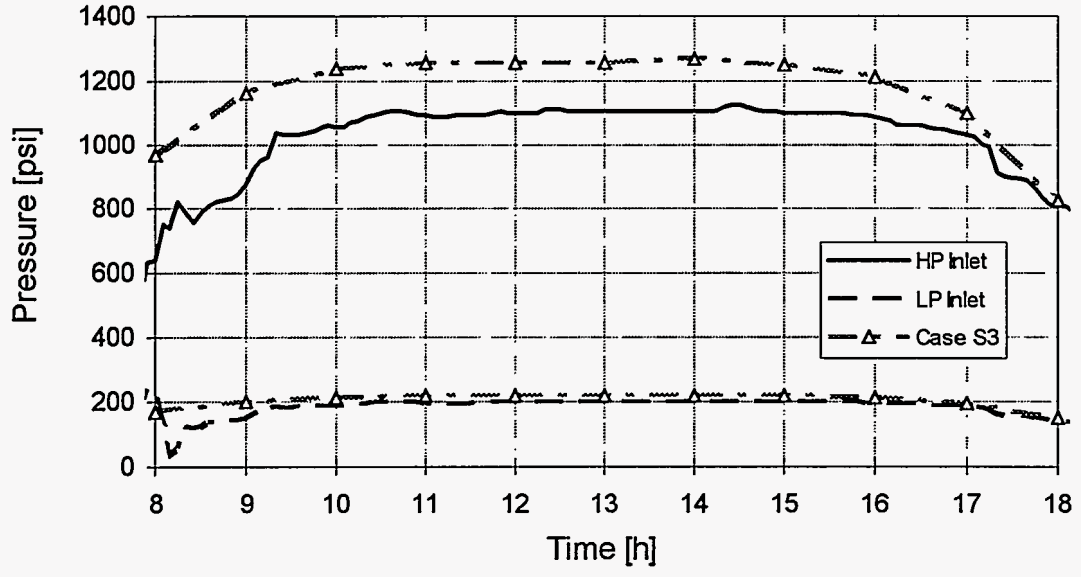

Fig.14b: Actual and predicted steam pressures during a clear summer day.

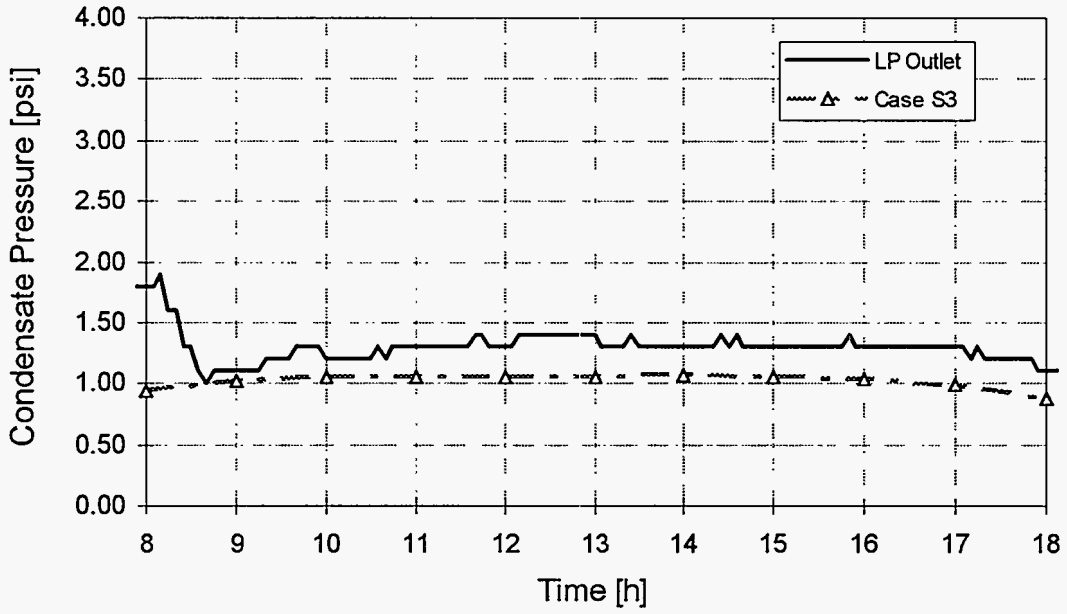

Fig.15b: Actual and predicted condensate back pressures during a clear summer day.

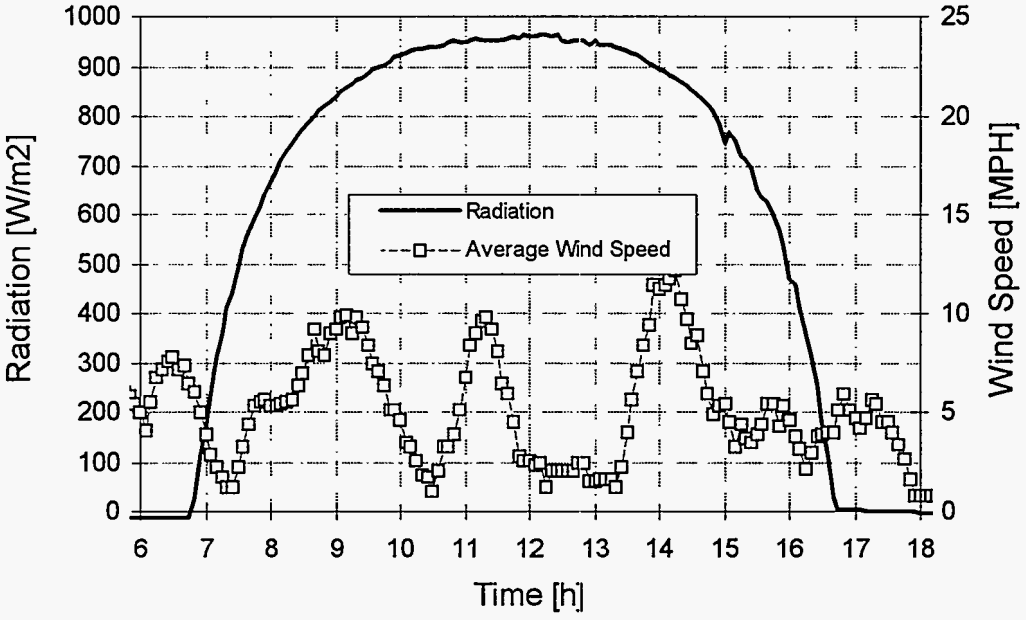

Fig. 17b: Insolation and wind speed during a clear winter day.

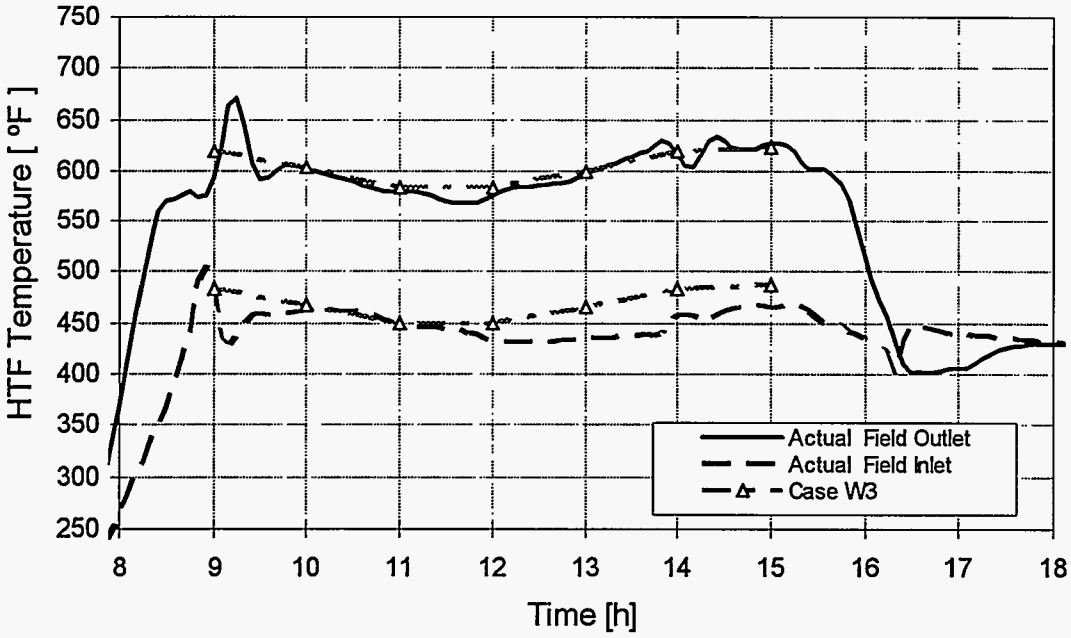

Fig.19b: HTF Temperatures during a clear winter day.

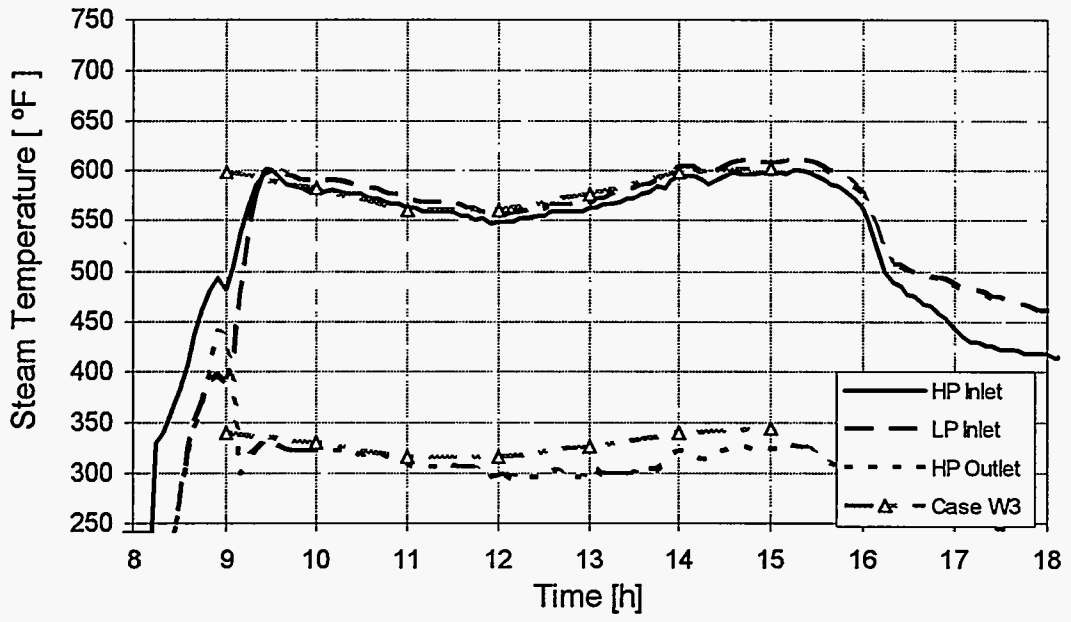

Fig.20b: Actual and predicted steam temperatures during a clear winter day.

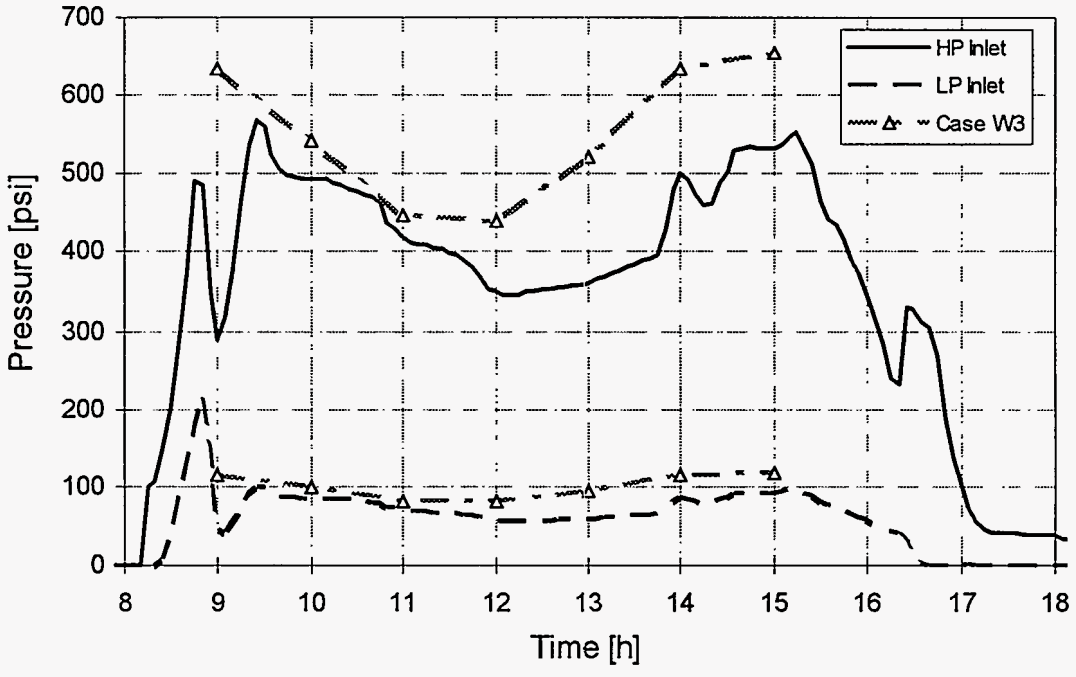

Fig.21b: Actual and predicted steam pressures during a clear winter day.

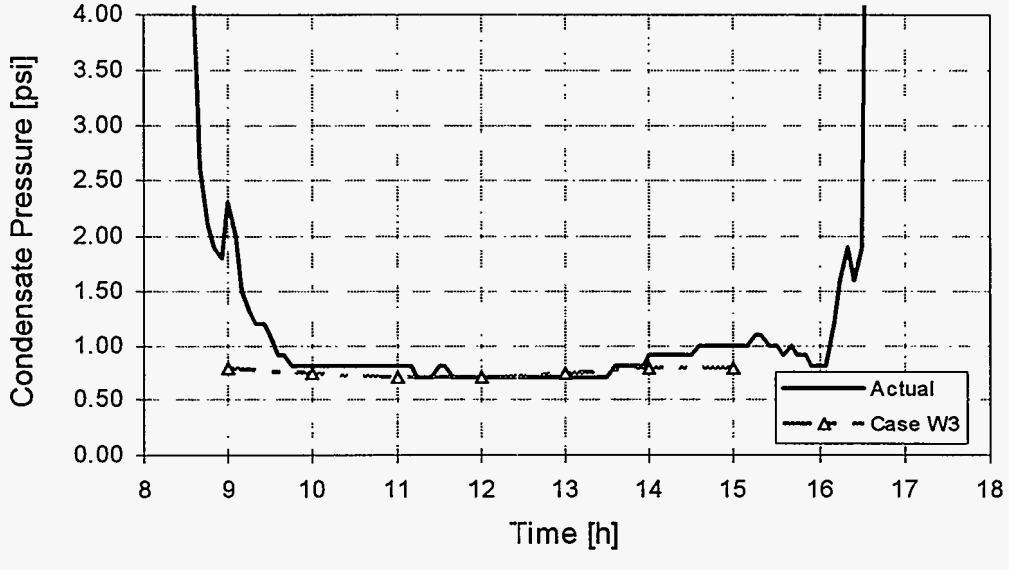

Fig.22b: Actual and predicted condensate pressures during a clear winter day.

David Hagen
134 Kitchener Street
Garran, ACT 2605, AUSTRALIA

3M - Solar Optics Program
Attn: Paul Jaster
3M Center
Building 225-2N-06
St. Paul, MN 55144-1000

Acurex Corporation
Attn: Hans Dehne
555 Clyde Avenue
Mountain View, CA 94039

Acurex Corporation
Attn: John Schaeffer
555 Clyde Avenue
Mountain View, CA 94039

Advanced Thermal Systems
Attn: Dave Gorman
7600 East Arapahoe Road, Suite 215
Englewood, CO 80112

Arizona Public Service Co.
Attn: Scott McLellan
P.O. Box 53999
MS 1424
Phoenix, AZ 85072-3999

Austrialian National University
Attn: Stephen Kaneff
Information Technology
0200 Canberra ACT, AUSTRALIA

Bechtel National, Inc.
Attn: Pascal (Pat) DeLaquil III
P. O. Box 193965
San Francisco, CA 94119-3965

Bechtel National, Inc.
Attn: Stuart Fry
50 Beale Street
50/15 D8
P.O. Box 193965
San Francisco, CA 94119-3965

Bechtel National, Inc.
Attn: Bruce Kelly
50 Beale Street
50/15 D25
P.O. Box 193965
San Francisco, CA 94119-3965

Bureau of Reclamation
Attn: Stanley Hightower
Code D-3710
P.O. Box 205007
Denver, CO 80225

California Energy Commission
Attn: Alec Jenkins
Energy Technology Development Div. R&D Office
1516 9th Street
MS-43
Sacramento, CA 95814-5512

California State Polytechnic University
Attn: William B. Stine
Department of Mechanical Engineering
3801 West Temple Avenue
Pomona, CA 91768-4062

Carrizo Solar Corporation
Attn: John Kusianovich
P.O. Box 10239
1011-C Sawmill Road NW
Albuquerque, NM 87184-0239

Central and South West Services
Attn: E. L. Gastineau
1616 Woodall Rogers Freeway
MS 7RES
Dallas, TX 75202

CIEMAT - PSA
Attn: Manuel Sanchez-Jimenez
Apartado 22
E-04200 Tabernas (Almeria), SPAIN

Daggett Leasing Corporation
Attn: Bill Ludlow
35100 Santa Fe St.
P.O. Box 373
Daggett, CA 92327

Daggett Leasing Corporation
Attn: Wayne Luton
35100 Santa Fe St.
P.O. Box 373
Daggett, CA 92327

Daggett Leasing Corporation
Attn: Eric Wills
35100 Santa Fe St.
P.O. Box 373
Daggett, CA 92327

DEO Enterprises
Attn: Dave Ochenreider
P.O. Box 2110
26443 Corona Drive
Helendale, CA 92342

DLR
Attn: Berthold Oberle
Pfaffenwaldring 38-40
7000 Stuttgart 80, GERMANY

DLR - Koln MD - ET
Attn: Manfred Becker
Linder Hohe
P.O. Box 90 60 58
D-51140 Koln, GERMANY

DLR - Koln MD - ET
Attn: Klaus Hennecke
Linder Hohe
P.O. Box 90 60 58
D-51147 Koln, GERMANY

Electric Power Research Institute
Attn: Dick Holl
1938A Avenida Del Oro
Oceanside, CA 92056

Electric Power Research Institute
Attn: Doug Morris
P.O. Box 10412
3412 Hillview Avenue
Palo Alto, CA 94303

Electric Power Research Institute
Attn: J. Schaeffer
P.O. Box 10412
3412 Hillview Avenue
Palo Alto, CA 94303

Fichtner Development Engineering GmbH
Attn: Peter Heinrich
Postfach 10 14 39
D-70013 Stuttgart, GERMANY

Florida Solar Energy Center
Attn: Library
300 State Road, Suite 401
Cape Canaveral, FL 32920-4099

Idaho Power
Attn: Jerry Young
P.O. Box 70
Boise, ID 83707

Industrial Solar Technology
Attn: Randy Gee
4420 McIntyre Street
Golden, CO 80403

Institute of Gas Technology
Attn: Library
34245 State Street
Chicago, IL 60616

Instituto de Investigaciones Electricas
Attn: Jorge M. Huacuz Villamar
Interior Internado Palmira
Apartado Postal 475
62000 Cuernavaca, Mor., MEXICO

Kearney & Associates
Attn: David W. Kearney (5)
14022 Condessa Drive
Del Mar, CA 92014

KJC Operating Company
Attn: Gilbert E. Cohen (5)
41100 Highway 395
Boron, CA 93516

Kramer Junction Company
Attn: Stuart Lawson
900 19th St. NW
Suite 600
Washington, DC 20006

Los Angeles Dept. of Water and Power
Attn: Daryl Yonamine
Alternate Energy Systems
111 North Hope Street, Rm. 661A
Los Angeles, CA 90012

McDonnell-Douglas Astronautics Co.
Attn: Bob Drubka
5301 Bolsa Avenue
Huntington Beach, CA 92647-2048

Ministry of Non-Conventional Energy Sources
Attn: S.K. Gupta
Block No. 14
CGO Complex
Lodhi Road
New Delhi, 110003 INDIA

Ministry of Non-Conventional Energy Sources
Attn: R.S. Sharma
Block No. 14
CGO Complex
Lodhi Road
New Delhi, 110003 INDIA

Ministry of Non-Conventional Energy Sources
Attn: Narendra Singh
Block No. 14
CGO Complex
Lodhi Road
New Delhi, 110003 INDIA

National Renewable Energy Laboratory
Attn: Mark Bohn
1617 Cole Blvd.
Branch 4710/132
Golden, CO 80401-3393

National Renewable Energy Laboratory
Attn: Hank Price (2)
1617 Cole Blvd.
Branch 4710/115
Golden, CO 80401-3393

National Renewable Energy Laboratory
Attn: Tim Wendelin
1617 Cole Blvd.
Branch 4710/105-11
Golden, CO 80401-3393

National Renewable Energy Laboratory
Attn: Tom Williams (6)
1617 Cole Blvd.
Branch 4700/118
Golden, CO 80401-3393

Nevada Power Co.
Attn: Eric Dominguez
P.O. Box 230
Las Vegas, NV 89151

Power Kinetics, Inc.
Attn: W.E. Rogers
415 River Street
Troy, NY 12180-2822

Renewable Energy Training Institute
Attn: Kevin Porter
122 C St. NW, Suite 520
Washington, DC 20001

Rockwell International Corp.
Attn: Bob Musica
Energy Technology Engineering Center
P.O. Box 1449
Canoga Park, CA 91304

Rockwell International Corp.
Attn: Bill Wahl
Rocketdyne Division
P.O. Box 7922
6633 Canoga Avenue
Canoga Park, CA 91309-7922

Sacramento Municipal Utility District
Attn: Bud Beebe
Generation Systems Planning
Power Systems Dept.
6201 'S' St.
P.O. Box 15830
Sacramento, CA 95852-1830

Sacramento Municipal Utility District
Attn: Don Osborne
Generation Systems Planning
Power Systems Dept.
6201 'S' St.
P.O. Box 15830
Sacramento, CA 95852-1830

Salt River Project
Attn: Bob Hess
Generation Engineering
P.O. Box 52025
Mail Station PAB358
Phoenix, AZ 85072-2025
Salt River Project
Attn: Ernie Palamino
Research & Development
P. O. Box 52025
Mail Station ISB664
Phoenix, AZ 85072-2025

SBP - Schlaich, Bergermann und. Partner
Attn: Wolfgang Schiel
Hohenzollernstr. 1
D-70178 Stuttgart, GERMANY

Science Applications International Corp.
Attn: Kelly Beninga
15000 W. 6th Avenue
Suite 202
Golden, CO 80401

Science Applications International Corp.
Attn: Barry L. Butler
Room 2043, M/S C2J
10260 Campus Point Dr.
San Diego, CA 92121

Science Applications International Corp.
Attn: Dave Smith
15000 W. 6th Avenue
Suite 202
Golden, CO 80401

Sloan Engineering
Attn: Michael Sloan
4306 Ramsey Ave.
Austin, TX 78756

Solar Energy Industries Association
Attn: Ken Sheinkopf
122 C Street, NW
4th Floor
Washington, DC 20001-2109

Solar Energy Industries Association
Attn: Scott Sklar
122 C Street., NW
4th Floor
Washington, DC 20001-2109

Solar Kinetics, Inc.
Attn: Gus Hutchison
10635 King William Drive
P.O. Box 540636
Dallas, TX 75354-0636

Solel Solar Systems, Ltd.
Attn: Har Hotzvim
Science-Based Park
P.O. Box 23577
Jerusalem, 91234 ISRAEL

South Coast AQMD
Attn: Ranji George
21865 Copley Drive
Diamond Bar, CA 91765

Southern California Edison Co.
Attn: Mark Skowronski
P.O. Box 800
2244 Walnut Grove Avenue
Rosemead, CA 91770

Southern California Edison Co.
Attn: Paul Sutherland
6090 Irwindale Avenue
Irwindale, CA 91702-3271

Spencer Management Associates
Attn: Byron J. Washom (5)
P.O. Box 724
Diablo, CA 94528-0724

Technology Properties Limited
Attn: Janet Neal
4010 Moorpark Avenue, Suite 215
San Jose, CA 95117

U.S. Department of Energy
Attn: Dan Alpert
2140 L Street, #709
Washington, DC 20037-1530

U.S. Department of Energy
Attn: R. (Bud) Annan (2)
Code EE-13
Forrestal Building
1000 Independence Ave. SW
Washington, DC 20585

U.S. Department of Energy
Attn: Gary Burch (5)
EE-132
Forrestal Building
1000 Independence Avenue, SW
Washington, DC 20585

U.S. Department of Energy
Attn: Bob Martin
Golden Field Office
1617 Cole Boulevard
Golden, CO 80401

UC Operating Services
Attn: Jan Hansen
43880 Harper Lake Road
Hinkley, CA 92347

Union of Concerned Scientists
Attn: Donald Aitken
20100 Skyline Boulevard
Woodside, CA 94062

University of Houston
Attn: Lorin Vant-Hull (2)
Energy Laboratory 5505
4800 Calhoun Road
Houston, TX 77004

University of Nevada at Las Vegas
Attn: Bob Boehm
Dept. of Mech. Engr.
4505 Maryland Parkway
P.O. Box 454027
Las Vegas, NV 89154-4027

Weizmann Institute of Science
Attn: Michael Epstein
P.O. Box 26
IS-76100 Rehovot, ISRAEL

Weizmann Institute of Science
Attn: Doron Lieberman
P.O. Box 26
Rehovot, 76100 ISRAEL

Zentrum fur Sonnenenergie-und Wasserstoff-Forschung
Attn: Frank Lippke
P.O. Box 801149
Stuttgart, D-705111 GERMANY

Zentrum fur Sonnenenergie-und Wasserstoff-Forschung
Attn: Jurgen Rheinlander (10)
Hessbruhlstrasse 21 C
Postfach 80 11 49
D-70511 Stuttgart, GERMANY

Internal Distribution:

MS 0100	Document Proc. for DOE/OSTI,7613-2
MS 0619	Technical Publications, 12613
MS 0702	Dan Arvizu, 6200
MS 0703	John Anderson, 6216
MS 0703	Chuck Andraka, 6216
MS 0703	Rich Diver, 6216
MS 0703	Don Gallup, 6216
MS 0703	Greg Kolb, 6216 (10)
MS 0703	Frank Lippke, 6216 (10)
MS 0703	Tom Mancini, 6216
MS 0703	Dave Menicucci, 6216
MS 0703	Jim Moreno, 6216
MS 0703	Tim Moss, 6216
MS 0703	Jim Pacheco, 6216
MS 0703	Michael Prairie, 6216
MS 0703	Craig Tyner, 6216
MS 0704	Paul Klimas, 6201
MS 0724	Dan Hartley, 6000
MS 0899	Technical Library, 13414
MS 1127	Jim Chavez, 6215
MS 1127	Vern Dudley, 6215
MS 1127	Library, 6215
MS 1127	Rod Mahoney, 6215
MS 9014	Scott Faas, 5371
MS 9018	Central Technical Files, 8523-2
MS 9402	Steve Goods, 8714
MS 9404	Bob Bradshaw, 8716